tides is striking. The deadenylation data also demonstrate that the ENE does not require the 3′ terminus of the poly(A) tail for binding, despite the involvement of the 3′ end of the A_9 RNA in the final base triple of the ENE core:A_9 structure. The results further argue that no specific register is required for the interaction of the wild-type ENE with the PAN RNA poly(A) tail. The presence of multiple binding sites for the ENE along the poly(A) sequence may contribute to its ability to protect tails of various lengths from deadenylation by cellular exonucleases (Fig. 4A). How the ENE may collaborate with poly(A)–binding proteins that are known to coat the poly(A) tails of RNA polymerase II transcripts in vivo (*25*) remains to be determined.

The key feature of the core ENE:A_9 crystal structure is a functionally important U-A•U major-groove triple helix, which is extended by A-minor interactions. The structure reveals an intramolecular clamp mechanism for recognition of poly(A) RNA and suggests how the ENE sequesters the PAN poly(A) tail from degradation by cellular deadenylases. Since viruses routinely borrow strategies from their hosts, we predict that similar mechanisms may protect some cellular noncoding RNAs from rapid turnover.

References and Notes

1. A. Viejo-Borbolla, M. Ottinger, T. F. Schulz, *Curr. HIV/AIDS Rep.* **1**, 5 (2004).
2. E. A. Mesri, E. Cesarman, C. Boshoff, *Nat. Rev. Cancer* **10**, 707 (2010).
3. D. M. Parkin *et al*., *Lancet Oncol.* **9**, 683 (2008).
4. R. Sun, S. F. Lin, L. Gradoville, G. Miller, *Proc. Natl. Acad. Sci. U.S.A.* **93**, 11883 (1996).
5. W. Zhong, H. Wang, B. Herndier, D. Ganem, *Proc. Natl. Acad. Sci. U.S.A.* **93**, 6641 (1996).
6. M. J. Song, H. J. Brown, T. T. Wu, R. Sun, *J. Virol.* **75**, 3129 (2001).
7. N. K. Conrad, J. A. Steitz, *EMBO J.* **24**, 1831 (2005).
8. N. K. Conrad, S. Mili, E. L. Marshall, M.-D. Shu, J. A. Steitz, *Mol. Cell* **24**, 943 (2006).
9. R. Parker, H. Song, *Nat. Struct. Mol. Biol.* **11**, 121 (2004).
10. A. C. Goldstrohm, M. Wickens, *Nat. Rev. Mol. Cell Biol.* **9**, 337 (2008).
11. N. K. Conrad, M.-D. Shu, K. E. Uyhazi, J. A. Steitz, *Proc. Natl. Acad. Sci. U.S.A.* **104**, 10412 (2007).
12. T. Kiss, E. Fayet-Lebaron, B. E. Jády, *Mol. Cell* **37**, 597 (2010).
13. Materials and methods are available as supporting material on *Science* Online.
14. Numbering from the 5′ end of the crystallization construct. ENE core nucleotides 1 to 16 correspond to PAN nucleotides 894 to 909, and 23 to 39 correspond to PAN nucleotides 943 to 959.
15. P. Nissen, J. A. Ippolito, N. Ban, P. B. Moore, T. A. Steitz, *Proc. Natl. Acad. Sci. U.S.A.* **98**, 4899 (2001).
16. E. A. Doherty, R. T. Batey, B. Masquida, J. A. Doudna, *Nat. Struct. Biol.* **8**, 339 (2001).
17. H. Jin, J. P. Loria, P. B. Moore, *Mol. Cell* **26**, 205 (2007).
18. H. Wu, J. Feigon, *Proc. Natl. Acad. Sci. U.S.A.* **104**, 6655 (2007).
19. C. A. Theimer, C. A. Blois, J. Feigon, *Mol. Cell* **17**, 671 (2005).
20. S. D. Gilbert, R. P. Rambo, D. Van Tyne, R. T. Batey, *Nat. Struct. Mol. Biol.* **15**, 177 (2008).
21. G. Felsenfeld, A. Rich, *Biochim. Biophys. Acta* **26**, 457 (1957).
22. G. Felsenfeld, D. Davies, A. Rich, *J. Am. Chem. Soc.* **79**, 2023 (1957).
23. D. J. D'Souza, E. T. Kool, *J. Biomol. Struct. Dyn.* **10**, 141 (1992).
24. The C-G•C base triple is strongest upon protonation of the Hoogsteen C nucleotide, but the triple helical structure can increase the pK_a of the C base, such that full protonation occurs at neutral pH (*19*).
25. U. Kühn, E. Wahle, *Biochim. Biophys. Acta* **1678**, 67 (2004).
26. N. B. Leontis, E. Westhof, *RNA* **7**, 499 (2001).
27. N.-K. Kim *et al*., *J. Mol. Biol.* **384**, 1249 (2008).
28. J. D. Dignam, R. M. Lebovitz, R. G. Roeder, *Nucleic Acids Res.* **11**, 1475 (1983).

29. We thank S. Borah, K. Tycowski, K. Herbert, and K. Riley for critical reading of the manuscript and the entire Steitz laboratories for helpful discussion. We thank S. Strobel and G. Conn for the generous gifts of iridium(III) hexamine and 3′-hepatitis delta virus (HDV) plasmid, respectively. Special thanks to Y. Zuo and G. Blaha for crystallography assistance, P. Moore and E. Paulson for NMR assistance, and M.-D. Shu, D. Mishler, and K. Durniak for technical assistance. X-ray data were collected at the National Synchrotron Light Source (X29A) at Brookhaven National Laboratory (*13*). Financial support for this research was provided by NIH grant CA16038 to J.A.S. and NIH grant GM022778 to T.A.S. The content is solely the responsibility of the authors and does not necessarily represent the official views of NIH. R.M.M.-F. is supported by a Jane Coffin Childs Memorial Fund Postdoctoral fellowship. J.A.S. and T.A.S. are investigators of the Howard Hughes Medical Institute. Coordinates and structure factors have been deposited in the Protein Data Bank under accession code 3P22.

Supporting Online Material

www.sciencemag.org/cgi/content/full/330/6008/1244/DC1
Materials and Methods
SOM Text
Figs. S1 to S8
Table S1

30 July 2010; accepted 15 October 2010
10.1126/science.1195858

PML Regulates Apoptosis at Endoplasmic Reticulum by Modulating Calcium Release

Carlotta Giorgi,[1,2,3,4] Keisuke Ito,[3,4] Hui-Kuan Lin,[4] Clara Santangelo,[5] Mariusz R. Wieckowski,[6] Magdalena Lebiedzinska,[6] Angela Bononi,[1] Massimo Bonora,[1] Jerzy Duszynski,[6] Rosa Bernardi,[3,4,7] Rosario Rizzuto,[8] Carlo Tacchetti,[5,9] Paolo Pinton,[1,3,4]* Pier Paolo Pandolfi[3,4]*

The promyelocytic leukemia (PML) tumor suppressor is a pleiotropic modulator of apoptosis. However, the molecular basis for such a diverse proapoptotic role is currently unknown. We show that extranuclear Pml was specifically enriched at the endoplasmic reticulum (ER) and at the mitochondria-associated membranes, signaling domains involved in ER-to-mitochondria calcium ion (Ca^{2+}) transport and in induction of apoptosis. We found Pml in complexes of large molecular size with the inositol 1,4,5-trisphosphate receptor (IP_3R), protein kinase Akt, and protein phosphatase 2a (PP2a). Pml was essential for Akt- and PP2a-dependent modulation of IP_3R phosphorylation and in turn for IP_3R-mediated Ca^{2+} release from ER. Our findings provide a mechanistic explanation for the pleiotropic role of Pml in apoptosis and identify a pharmacological target for the modulation of Ca^{2+} signals.

The promyelocytic leukemia gene (*PML*) was originally identified at the breakpoint of the t(15;17) translocation of acute promyelocytic leukemia (APL), and function of the PML protein is frequently lost or aberrant in human solid tumors and hematopoietic malignancies (*1*, *2*). PML is a nuclear protein and an essential component of subnuclear structures termed nuclear bodies (NBs) (*3*). However, many, if not all, PML isoforms have shown both cytoplasmic and nuclear localization (*4*, *5*). $Pml^{-/-}$ mice and primary cells are protected from apoptosis triggered by a number of diverse stimuli (*6*).

To determine how PML could regulate such broadly diverse apoptotic responses, we analyzed its intracellular localization by cell fractionation (*7*, *8*). We fractionated homogenates of primary mouse embryonic fibroblasts (MEFs) by ultracentrifugation, focusing on the mitochondria, endoplasmic reticulum (ER), and mitochondria-associated membranes (MAMs), the structures that contain sites where the ER contacts mitochondria. Pml localized both to the nucleus and the cytosol and appeared to localize also to the ER, MAM, and crude mitochondrial fractions but not to "pure" mitochondrial fraction free of ER and nuclear markers (Fig. 1A). These results were confirmed by immunogold labeling of ultrathin cryosections showing that Pml associates with the surface of the ER (Fig. 1B, a and b) and in the proximity of

[1]Department of Experimental and Diagnostic Medicine, Section of General Pathology, Interdisciplinary Center for the Study of Inflammation (ICSI), Emilia Romagna Laboratory BioPharmaNet, and Laboratory for Technologies of Advanced Therapies (LTTA) University of Ferrara, Ferrara, Italy. [2]Vita-Salute San Raffaele University, Center of Excellence in Cell Development, and IIT Network, Research Unit of Molecular Neuroscience, Milan, Italy. [3]Cancer Genetics Program, Beth Israel Deaconess Cancer Center, Departments of Medicine and Pathology, Beth Israel Deaconess Medical Center, Harvard Medical School, Boston, MA 02215, USA. [4]Cancer Biology and Genetics Program, Department of Pathology, Memorial Sloan-Kettering Cancer Center, New York, NY 10065, USA. [5]IFOM (FIRC Institute of Molecular Oncology Foundation) Centre of Cell Oncology and Ultrastructure MicroSCoBiO Research Center, Department of Experimental Medicine, University of Genova, Genova, Italy. [6]Nencki Institute of Experimental Biology, Warsaw, Poland. [7]San Raffaele Research Institute, Department of Molecular Oncology, Milan, Italy. [8]Department of Biomedical Sciences, University of Padua, Padua, Italy. [9]Scientific Institute San Raffaele, Experimental Imaging Center, Milan, Italy.

*To whom correspondence should be addressed. E-mail: ppandolf@bidmc.harvard.edu (P.P.P.); pnp@unife.it (P.P.)

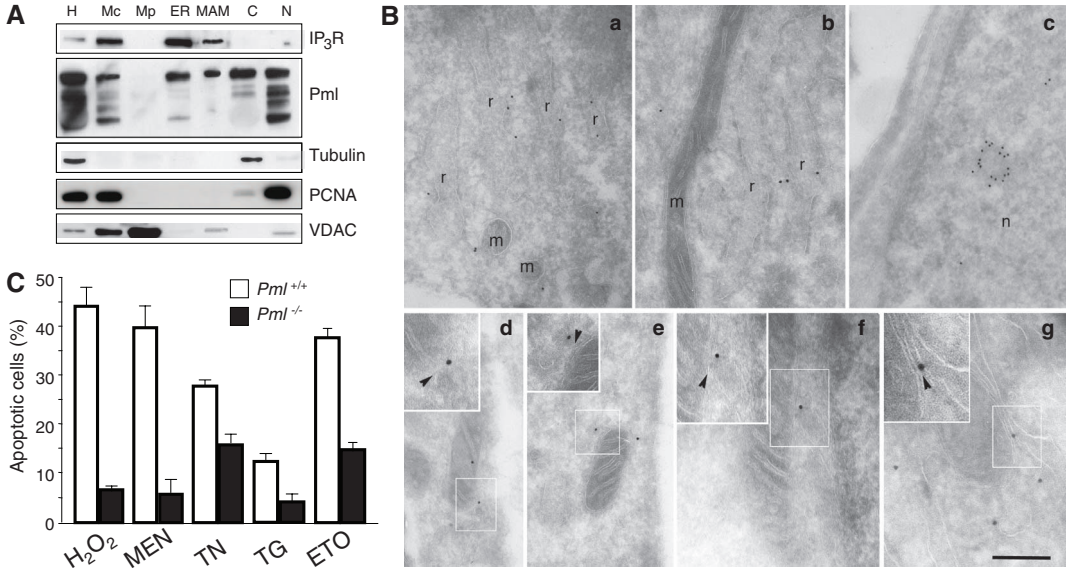

Fig. 1. Identification of Pml at ER and MAM regions and Ca^{2+}-mediated Pml-dependent cell death. (**A**) Detection of Pml by immunoblotting in $Pml^{+/+}$ MEFs fractionation. IP_3R, tubulin, proliferating cell nuclear antigen (PCNA), and voltage-dependent anion channel (VDAC) are used as markers. H: homogenate; Mc: crude mitochondria; Mp: pure mitochondria; ER; MAM; C: cytosol; N: nucleus. (**B**) Immunogold labeling of Pml near the rough ER (r), mitochondria (m), and MAM (arrowheads) in $Pml^{+/+}$ MEFs. Gold particles (15 nm) are mostly associated with the surface of the ER (7.07 gold particles/μm^2) and more occasionally with mitochondrial membranes (3.08 gold particles/μm^2) (a and b). Specificity of the antibodies is demonstrated by labeling of nuclear bodies (n) (c). Morphologically identified MAM often demonstrated labeling at contacts between ER and mitochondria [(d) to (g), and arrowheads in insets therein]. Insets correspond to boxed areas. Bar: (a) 360 nm; (b) 340 nm; (c) 370 nm; (d) 188 nm, inset 120 nm; (e) 260 nm, inset 190 nm; (f) 340 nm, inset 180 nm; (g) 280 nm, inset 210 nm. (**C**) Apoptosis induced by 1 mM H_2O_2, 15 μM menadione (MEN), 6 μM tunicamycin (TN), 2 μM thapsigargin (TG), or 50 μM etoposide (ETO) in $Pml^{+/+}$ or $Pml^{-/-}$ MEFs treated for 12 hours. Data represent the mean SD of five independent experiments.

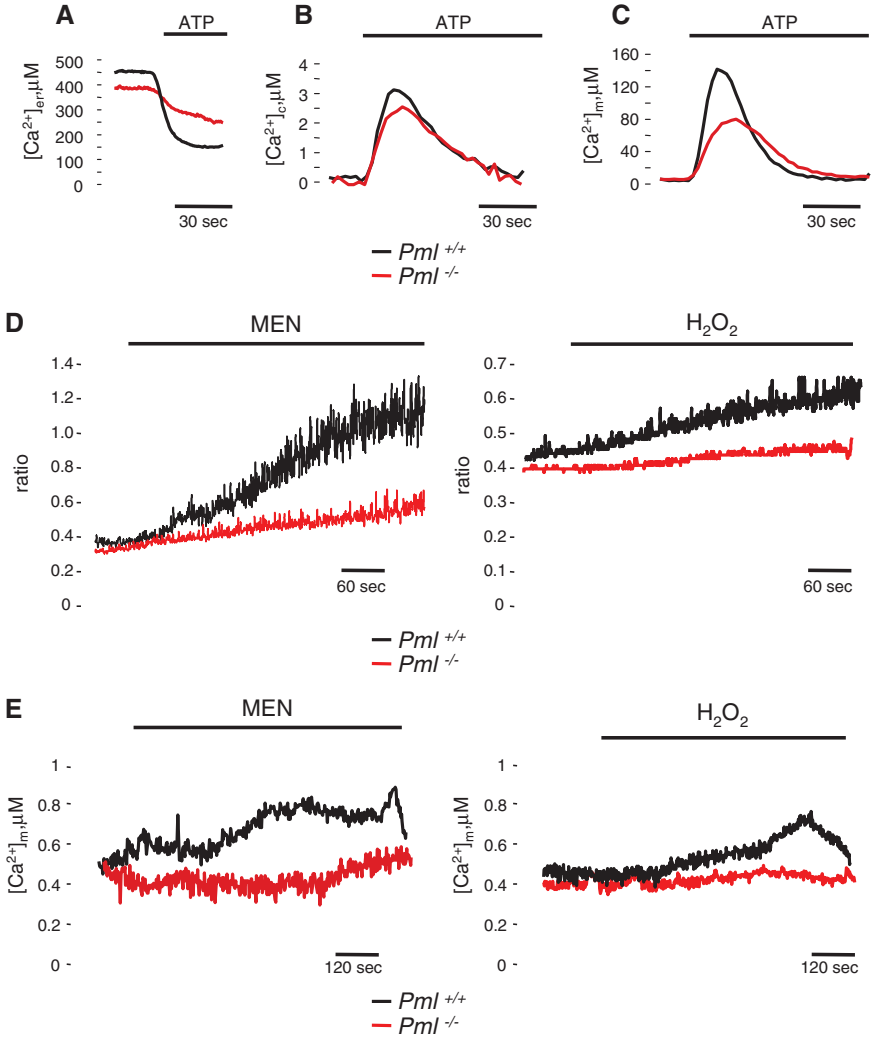

Fig. 2. Intracellular Ca^{2+} homeostasis in $Pml^{+/+}$ and $Pml^{-/-}$ MEFs. (**A** to **C**) ER (A), cytosolic (B), and mitochondrial (C) Ca^{2+} homeostasis measurements with aequorins. Where indicated, cells were treated with 100 μM ATP. $Pml^{+/+}$: $[Ca^{2+}]_{ER}$ peak 448 ± 32 μM; $[Ca^{2+}]_c$ peak 3.3 ± 0.16 μM; $[Ca^{2+}]_m$ peak 138 ± 14 μM. $Pml^{-/-}$: $[Ca^{2+}]_{ER}$ peak 386 ± 42 μM; $[Ca^{2+}]_c$ peak 2.65 ± 0.23 μM; $[Ca^{2+}]_m$ peak 78 ± 10 μM. $n = 15$ samples from five independent experiments, $P < 0.01$. (**D**) MEFs loaded with calcium-sensitive fluorescent dye fura-2 were stimulated with menadione (MEN) or H_2O_2. The kinetic behavior of the $[Ca^{2+}]_c$ response is presented as the ratio of fluorescence at 340 nm/380 nm. In these, and other fura-2 experiments, the traces are representative of at least 10 single-cell responses from three independent experiments. (**E**) Analysis of $[Ca^{2+}]_m$ during oxidative stress. Where indicated, cells were stimulated with 30 μM MEN or 2 mM H_2O_2. $n = 10$ samples from three independent experiments.

the mitochondrial membrane at contact sites between the ER and mitochondria (Fig. 1B, d to g).

In view of the localization of Pml at the ER and MAM, we investigated its requirement in apoptosis induced by ER stress (*9*). Matched wild-type ($Pml^{+/+}$) and $Pml^{-/-}$ MEFs were treated with ER stress inducers: H_2O_2 and menadione (MEN), two oxidizing agents that induce ER Ca^{2+} release; tunicamycin (TN) or an inhibitor of protein N-glycosylation; and thapsigargin (TG), an inhibitor of the sarcoplasmic/ER Ca^{2+}-ATPase (adenosine triphosphatase). After 12 hours of treatment, the percentage of apoptotic cells in $Pml^{-/-}$ MEFs was much lower than that observed in $Pml^{+/+}$ MEFs under all treatment conditions (Fig. 1C and fig. S1).

MAMs are specialized domains selectively enriched in critical Ca^{2+} signaling elements, which mediate Ca^{2+} transfer between ER and mitochondria (*10*, *11*), such as the inositol 1,4,5-trisphosphate receptor (IP_3R) (*12*). Ca^{2+} signaling has a major role in the regulation of cell death (*13*, *14*). Release of the ER Ca^{2+} pool through the type 3 IP_3R (IP_3R3) appears to induce a sensitization of cells to apoptotic stimuli (*15*, *16*).

To investigate the role of Pml in Ca^{2+} homeostasis, we used recombinant Ca^{2+}-sensitive bioluminescent protein aequorin (*17*). In $Pml^{+/+}$ MEFs, the Ca^{2+} concentration ($[Ca^{2+}]$) in the lumen of the ER ($[Ca^{2+}]_{ER}$) at steady state was ~450 μM, whereas in $Pml^{-/-}$ MEFs it was lower. When the cells were stimulated with adenosine 5′-triphosphate (ATP), the P2Y receptor agonist that causes release of Ca^{2+} from the ER, the decreases in the $[Ca^{2+}]_{ER}$ observed in $Pml^{+/+}$ MEFs in quantitative and kinetic terms were larger and faster than in $Pml^{-/-}$ MEFs, reflecting a more rapid flow of Ca^{2+} through the IP_3R (Fig. 2A). In turn, the $[Ca^{2+}]$ increases evoked by stimulation with ATP in the cytosol ($[Ca^{2+}]_c$) and mitochondria ($[Ca^{2+}]_m$) were smaller in $Pml^{-/-}$ than in $Pml^{+/+}$ MEFs (Fig. 2, B and C, and fig. S2). A mitochondrial Ca^{2+} deregulation was observed also in human-derived cells in which PML was depleted (fig. S3) and in different cellular models of APL (fig. S4).

We then investigated whether the absence of Pml could alter the increases in $[Ca^{2+}]_c$ and $[Ca^{2+}]_m$ induced by apoptotic stimuli. In $Pml^{-/-}$ MEFs, the increases in $[Ca^{2+}]_c$ and $[Ca^{2+}]_m$, evoked by the oxidative apoptotic stimuli, such as MEN and H_2O_2 that trigger both a progressive release of Ca^{2+} from the ER and an activation of the capacitative Ca^{2+} influx (*18*), were smaller as mentioned above (Fig. 2, D and E).

To determine whether the effects of Pml on regulation of Ca^{2+} homeostasis depend on its localization to the ER and MAMs, we generated a chimeric protein containing the entire PML protein that was targeted to the outer surface of the ER (*19*). This chimera, designated erPML, localized to the ER and MAMs in $Pml^{-/-}$ MEFs, as revealed by immunocytochemical staining, immunogold labeling, and subfractionation (Fig. 3A and fig. S5). The introduction of erPML in $Pml^{-/-}$ MEFs restored Ca^{2+} signals evoked by either agonist (Fig. 3B and fig. S6) or apoptotic stimuli (MEN or H_2O_2) (Fig. 3C) to values comparable to

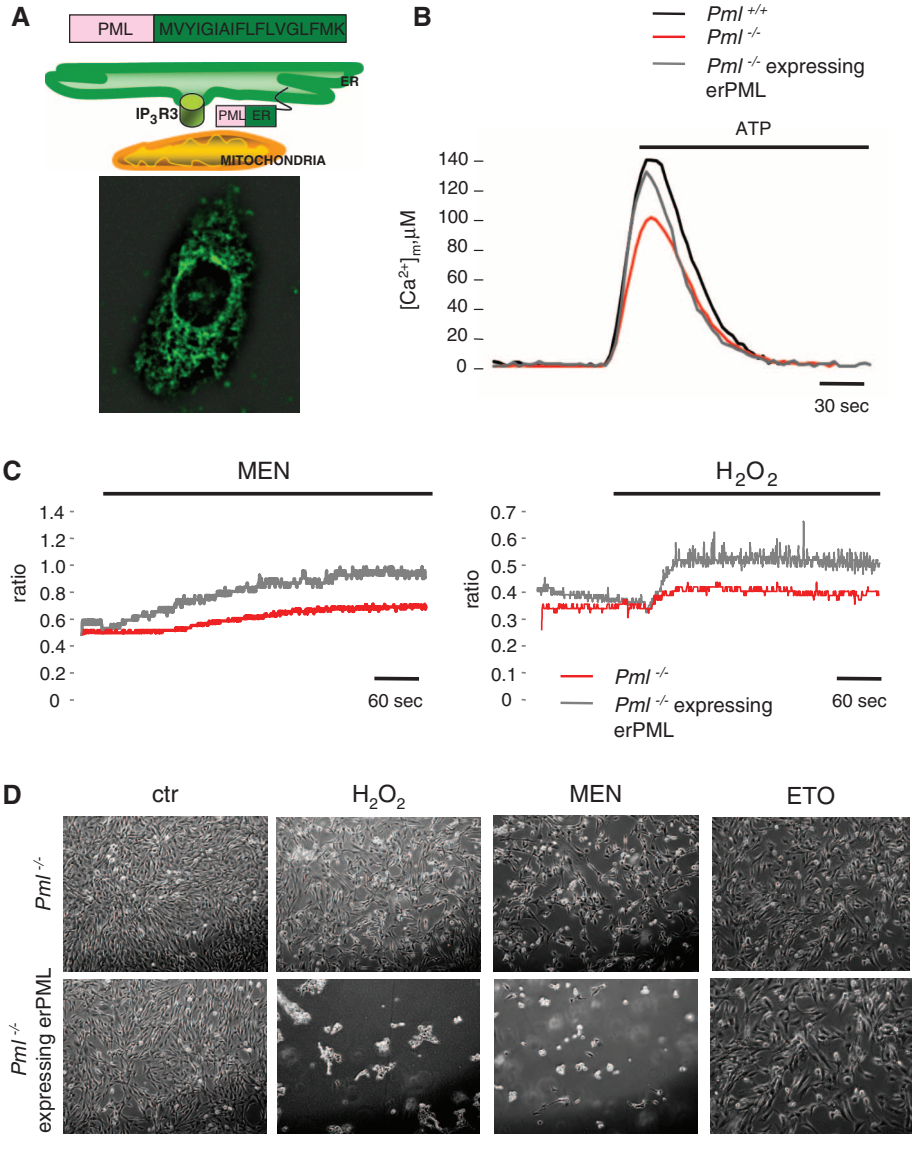

Fig. 3. erPML chimera reestablishes the $[Ca^{2+}]_m$ and apoptotic responses in $Pml^{-/-}$ MEFs. (**A**) Schematic map of the erPML chimera and immunofluorescence image, stained with the antibody to PML, of $Pml^{-/-}$ MEFs expressing erPML. (**B**) erPML reestablishes the agonist-dependent $[Ca^{2+}]_m$ response in $Pml^{-/-}$ MEFs ($[Ca^{2+}]_m$ peak 135 ± 12 μM) to values comparable to those of $Pml^{+/+}$ MEFs. (**C**) $Pml^{-/-}$ and $Pml^{-/-}$ MEFs expressing erPML previously incubated with fura-2 were stimulated with menadione (MEN) or H_2O_2. (**D**) Representative microscopic fields of $Pml^{-/-}$ MEFs and $Pml^{-/-}$ expressing erPML before and after treatment with 1 mM H_2O_2, 15 μM MEN, or 50 μM etoposide (ETO) for 16 hours.

those in *Pml*$^{+/+}$ MEFs (Fig. 2, C and D). This effect was associated with a reestablished sensitivity to apoptosis induced by ER stress but did not restore the sensitivity to etoposide (ETO) (Fig. 3D and fig. S7A), a DNA-damaging agent that triggers apoptotic death by a Ca^{2+}-independent process (fig. S7B). Overall, these experiments indicate that the absence of Pml causes a reduction in the amplitude of Ca^{2+} signals induced by ATP, other agents, or apoptotic stimuli, and that forcing PML to the ER rescues these defects. A PML protein targeted to the nucleus restored the formation of NBs, but did not restore the Ca^{2+} responses and the sensitivity to ER stress–dependent cell death, although it restored response to other apoptotic stimuli such as ETO (fig. S8).

To investigate the mechanism underlying these activities of Pml, we tested whether Pml could functionally and physically interact with the IP_3R3. Immunoprecipitation of IP_3R3 led to the coprecipitation of Pml (Fig. 4A and fig. S9) and vice versa (fig. S10). Amounts of phosphorylated-IP_3R3 (p-IP_3R3) were higher in *Pml*$^{-/-}$ than in *Pml*$^{+/+}$ MEFs (Fig. 4A and fig. S11).

Reduced cellular sensitivity to apoptotic stimuli was observed in cells with high activity of the protein kinase Akt, as a result of diminished Ca^{2+} flux from the ER through the IP_3R (*20*, *21*). The amount of phosphorylated Akt (pAkt) (that is, the active form of Akt) coprecipitated with IP_3R3 (Fig. 4A and fig. S9) was higher in *Pml*$^{-/-}$ than in *Pml*$^{+/+}$ MEFs (fig. S11). Dephosphorylation of Akt at the MAM might occur through Pml-mediated recruitment of the phosphatase PP2a. Indeed, Pml interacts with PP2a in Pml-NBs (*22*). Further, the amount of PP2a coprecipitated with IP_3R3 (Fig. 4A and figs. S9 and S10) was diminished in *Pml*$^{-/-}$ MEFs (Fig. 4A and fig. S11). Thus, in the absence of *Pml*, reduced Ca^{2+} release could be caused by increased phosphorylation and activation of Akt at the ER due to an impaired PP2a activity, which in turn impair Ca^{2+} flux through the IP_3R because of its hyperphosphorylated state (figs. S11 and S12).

To determine whether IP_3R3, Pml, Akt, and PP2a interact in a complex, we next performed two-dimensional blue native analysis. We found that Pml, IP_3R3, Akt, and PP2a colocalize in high molecular weight complexes, supporting their possible interaction in the native state (fig. S13). Finally, we demonstrated the localization of all these proteins at the ER and MAM through immunocytochemical staining and subfractionation (Fig. 4, B and C, and fig. S14).

We further investigated the correlation among Pml, Akt, and PP2a at the ER and the regulation of the IP_3R by a selective inhibition of either Akt or PP2a. Pretreatment of cells with okadaic acid (OA, a PP2a inhibitor) caused a reduction in $[Ca^{2+}]_m$ responses to ATP stimulation and a reduced H_2O_2- or MEN-induced death in *Pml*$^{+/+}$ MEFs and in *Pml*$^{-/-}$ MEFs expressing erPML, but not in *Pml*$^{-/-}$ MEFs (Fig. 4, D and E, and figs. S15, S16, and S18), in which PP2a activity is impaired. LY294002 (an inhibitor of Akt) had no

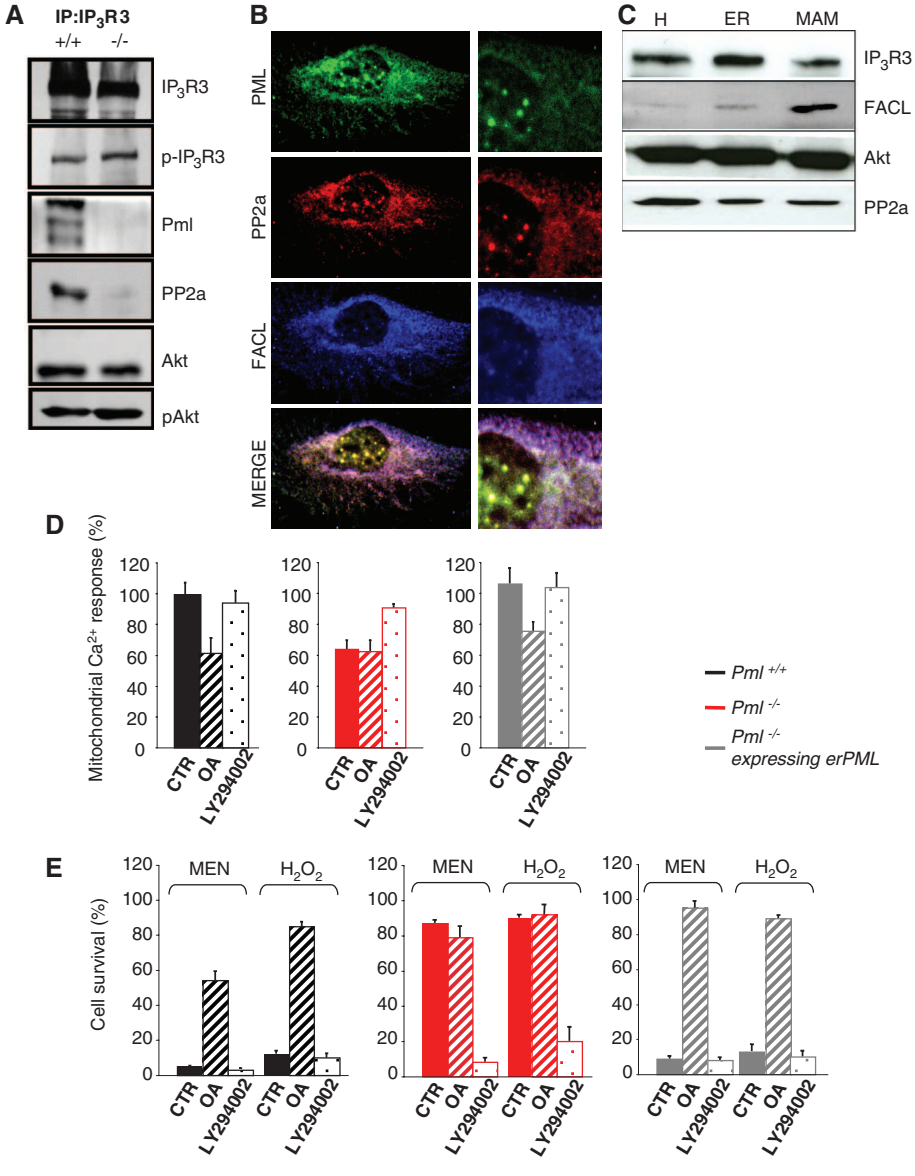

Fig. 4. Modulation of $[Ca^{2+}]_m$ and apoptotic responses by Pml through Akt- and PP2a-dependent phosphorylation of IP_3R3. (**A**) Coimmunoprecipitation of IP_3R3 with Pml, Akt, and PP2a in *Pml*$^{+/+}$ MEFs. In the same blot, the levels of p-IP_3R3 and pAkt are shown. (**B**) Localization of Pml (green) and PP2a (red) at ER and MAM sites in *Pml*$^{+/+}$ MEFs analyzed by immunofluorescence. FACL [long-chain fatty acid–CoA (coenzyme A) ligase type 4, blue] was used as MAM marker. (**C**) *Pml*$^{+/+}$ MEFs subcellular fractionation and identification of PP2a and Akt at ER and MAM fractions by immunoblot. (**D**) Effects of okadaic acid (OA, 1 μM for 1 hour) and LY294002 (5 μM for 30 min) on agonist-dependent $[Ca^{2+}]_m$ responses in *Pml*$^{+/+}$, *Pml*$^{-/-}$, and *Pml*$^{-/-}$ MEFs expressing erPML. $[Ca^{2+}]_m$ is represented as a percentage of the peak value of control cells. Representative traces are shown in fig. S15. (**E**) Quantification of cell survival of *Pml*$^{+/+}$, *Pml*$^{-/-}$, and *Pml*$^{-/-}$ MEFs expressing erPML, control (CTR, untreated) and treated first with OA (1 μM for 1 hour) or LY294002 (5 μM for 30 min) and then H_2O_2 or menadione (MEN) for 16 hours. The data show the percentage of living cells in the whole-cell population negative for annexin-V–fluorescein isothiocyanate and propidium iodide staining, analyzed by flow cytometry. Data show the means SD from three independent experiments.

effect on the agonist-dependent $[Ca^{2+}]_m$ transients and on apoptosis in $Pml^{+/+}$ or $Pml^{-/-}$ MEFs expressing erPML, whereas it increased agonist-dependent $[Ca^{2+}]_m$ responses and restored sensitivity to H_2O_2 or MEN (Fig. 4, D and E, and figs. S15, S17, and S18) in $Pml^{-/-}$ MEFs (in which high levels of pAkt are observed; Fig. 4A and fig. S11). These results were confirmed in experiments in which RNA interference was used to deplete cells of Akt or PP2a proteins (fig. S19, A and B) or a constitutively active form of Akt (m/p Akt) was expressed (fig. S19C).

Our data highlight an extranuclear, transcription-independent function of Pml that regulates cell survival through changes in Ca^{2+} signaling in the ER, cytosol, and mitochondria (fig. S20). This effect appears to be specific to Ca^{2+}-mediated apoptotic stimuli because alteration in Pml did not influence cell death in cells treated with ETO, which activates the apoptotic pathway in a way largely independent of Ca^{2+}.

This mechanism may explain how Pml can so broadly regulate the early (and transcription independent) apoptotic response. Our findings may have implications in tumorigenesis where the function of Pml is frequently lost, or in other pathophysiological conditions where Pml is accumulated such as cell stress, or infection with viral or bacterial pathogens.

References and Notes

1. P. Salomoni, P. P. Pandolfi, *Cell* **108**, 165 (2002).
2. C. Gurrieri *et al.*, *J. Natl. Cancer Inst.* **96**, 269 (2004).
3. T. H. Shen, H. K. Lin, P. P. Scaglioni, T. M. Yung, P. P. Pandolfi, *Mol. Cell* **24**, 331 (2006).
4. H. K. Lin, S. Bergmann, P. P. Pandolfi, *Nature* **431**, 205 (2004).
5. W. Condemine *et al.*, *Cancer Res.* **66**, 6192 (2006).
6. R. Bernardi, A. Papa, P. P. Pandolfi, *Oncogene* **27**, 6299 (2008).
7. M. R. Wieckowski, C. Giorgi, M. Lebiedzinska, J. Duszynski, P. Pinton, *Nat. Protoc.* **4**, 1582 (2009).
8. Materials and methods are available as supporting material on *Science* Online.
9. C. Giorgi, D. De Stefani, A. Bononi, R. Rizzuto, P. Pinton, *Int. J. Biochem. Cell Biol.* **41**, 1817 (2009).
10. P. Pinton, C. Giorgi, R. Siviero, E. Zecchini, R. Rizzuto, *Oncogene* **27**, 6407 (2008).
11. T. Hayashi, R. Rizzuto, G. Hajnoczky, T. P. Su, *Trends Cell Biol.* **19**, 81 (2009).
12. R. L. Patterson, D. Boehning, S. H. Snyder, *Annu. Rev. Biochem.* **73**, 437 (2004).
13. C. Giorgi, A. Romagnoli, P. Pinton, R. Rizzuto, *Curr. Mol. Med.* **8**, 119 (2008).
14. D. E. Clapham, *Cell* **131**, 1047 (2007).
15. P. Pinton, R. Rizzuto, *Cell Death Differ.* **13**, 1409 (2006).
16. C. C. Mendes *et al.*, *J. Biol. Chem.* **280**, 40892 (2005).
17. P. Pinton, A. Rimessi, A. Romagnoli, A. Prandini, R. Rizzuto, *Methods Cell Biol.* **80**, 297 (2007).
18. P. Pinton *et al.*, *EMBO J.* **20**, 2690 (2001).
19. M. Yang, J. Ellenberg, J. S. Bonifacino, A. M. Weissman, *J. Biol. Chem.* **272**, 1970 (1997).
20. T. Szado *et al.*, *Proc. Natl. Acad. Sci. U.S.A.* **105**, 2427 (2008).
21. S. Marchi *et al.*, *Biochem. Biophys. Res. Commun.* **375**, 501 (2008).
22. L. C. Trotman *et al.*, *Nature* **441**, 523 (2006).

23. This work was supported in part by grants from the National Cancer Institute (to P.P.P.); by K99 NIH (to I.K.); by AIRC, FISM, Telethon, Ministry of Health, and PRIN (to P.P.); by FP7 "MyoAGE", NIH, Cariparo Foundation, and AIRC (to R. R.); and by grants from the Ministry of Science and Higher Education in Poland and the Polish Mitochondrial Network (to M.L., J.D., and M.R.W.). We thank S. Missiroli, F. Poletti, and C. Agnoletto for carrying out some experiments, and J. Meldolesi and members of the Pandolfi and Pinton lab for stimulating discussions.

Supporting Online Material

www.sciencemag.org/cgi/content/full/science.1189157/DC1
Materials and Methods
Figs. S1 to S20
References

5 March 2010; accepted 13 October 2010
Published online 28 October 2010;
10.1126/science.1189157

Reprogramming Cellular Behavior with RNA Controllers Responsive to Endogenous Proteins

Stephanie J. Culler,[1] Kevin G. Hoff,[1] Christina D. Smolke[1,2]*

Synthetic genetic devices that interface with native cellular pathways can be used to change natural networks to implement new forms of control and behavior. The engineering of gene networks has been limited by an inability to interface with native components. We describe a class of RNA control devices that overcome these limitations by coupling increased abundance of particular proteins to targeted gene expression events through the regulation of alternative RNA splicing. We engineered RNA devices that detect signaling through the nuclear factor κB and Wnt signaling pathways in human cells and rewire these pathways to produce new behaviors, thereby linking disease markers to noninvasive sensing and reprogrammed cellular fates. Our work provides a genetic platform that can build programmable sensing-actuation devices enabling autonomous control over cellular behavior.

Cellular decisions, such as differentiation, response to stress, disease progression, and apoptosis, depend on regulatory networks that control enzymatic activities, protein translocation, and genetic responses. Central to the genetic programming of biological systems is the ability to process information within cellular networks and link this information to new cellular behaviors, in essence rewiring network topologies. Altered network topologies have been achieved through engineered transcriptional networks (*1*, *2*) and signal transduction cascades (*3*). However, these systems are limited to processing transcription-factor inputs, which represent a small fraction of the human proteome (*4*, *5*) or require replacing endogenous cellular components. Alternative platforms for constructing sensing-actuation devices based on the detection of broad classes of proteins will have widespread applications in basic research, biotechnology, and medicine.

RNA is a promising substrate for platforms to interface with cellular networks because of the versatile sensing and actuation functions that RNA can exhibit and the ease with which RNA structures can be designed (*6*, *7*). RNA-based sensing-actuation devices have been engineered that respond predominantly to externally applied small-molecule (*6*, *8*, *9*) and nucleic acid (*10*–*12*) inputs and control gene expression through diverse mechanisms. Pre-mRNA splicing is one such mechanism, in which devices responsive to exogenous small-molecule and protein inputs can regulate splicing events (*8*, *13*). However, protein-responsive gene regulatory platforms based on programmed alternative splicing must support modular and extensible input/output functionalities, provide regulatory properties that translate to control over cell behaviors, and be sensitive to changes in endogenous protein concentrations or localization. Although RNA aptamers that bind to proteins have been generated through in vitro selection methods (*14*, *15*), such protein-sensing components have not been routinely integrated into RNA-based regulatory devices, leaving a large number of biological signals currently inaccessible.

We developed a protein-responsive RNA-based regulatory device by integrating RNA aptamers that bind to protein ligands in key intronic locations of an alternatively spliced transcript, thus linking intracellular protein concentrations to gene-expression events (*16*). Our regulatory platform consists of an output module, or a gene of interest (GOI) placed downstream of the sensing-actuation device, and a three-exon, two-intron minigene in which the middle exon is alternatively spliced or excluded (Fig. 1A). The middle exon contains a stop codon, such that expression of the GOI is high when the exon is excluded. Control is exerted by the input module, composed of an RNA aptamer that senses changes in nuclear protein concentrations whereby ligand binding to the

[1]Division of Chemistry and Chemical Engineering, 1200 East California Boulevard, MC 210-41, California Institute of Technology, Pasadena, CA 91125, USA. [2]Department of Bioengineering, 473 Via Ortega, MC 4201, Stanford University, Stanford, CA 94305, USA.

*To whom correspondence should be addressed. E-mail: csmolke@stanford.edu

www.sciencemag.org/cgi/content/full/science.1189157/DC1

Supporting Online Material for

PML Regulates Apoptosis at Endoplasmic Reticulum by Modulating Calcium Release

Carlotta Giorgi, Keisuke Ito, Hui-Kuan Lin, Clara Santangelo, Mariusz R. Wieckowski, Magdalena Lebiedzinska, Angela Bononi, Massimo Bonora, Jerzy Duszynski, Rosa Bernardi, Rosario Rizzuto, Carlo Tacchetti, Paolo Pinton,* Pier Paolo Pandolfi*

*To whom correspondence should be addressed. E-mail: ppandolf@bidmc.harvard.edu (P.P.P.); pnp@unife.it (P.P)

Published 28 October 2010 on *Science* Express
DOI: 10.1126/science.1189157

This PDF file includes:

Supporting online material

Materials and Methods

Reagents and solutions

ATP, luciferin, digitonin, H_2O_2, menadione (MEN), tunycamicin (TN), thapsigargin (TG), etoposide (ETO), okadaic acid (OA), LY294002 and arsenic trioxide (As_2O_3) were purchased from Sigma, coelenterazine from Molecular Probes.
KRB contained: 125 mM NaCl, 5 mM KCl, 1 mM $MgSO_4$, 1 mM Na_2HPO_4, 5.5 mM glucose, 20 mM $NaHCO_3$, 2 mM l-glutamine and 20 mM HEPES pH 7.4, and was supplemented with 1 mM $CaCl_2$.

Cells culture, transfection, infection and detection of cell death

Primary *Pml*$^{+/+}$ and *Pml*$^{-/-}$ MEFs were prepared from embryos at day 13.5 of development (E13.5). Early passage (P2–P5) MEFs, grown in DMEM supplemented with 10% FCS, were used in all experiments.
MEFs were transfected with different constructs using the MicroPorator (Digital Bio).
Human kidney cells (HEK) were grown in DMEM supplemented with 10% FCS and transfected with a standard calcium-phosphate procedure. siRNA of PML in a retrovirus vector (pBABE) was used for PML depletion in HEK cells.
shRNA lentiviral transduction particles (cloned into the pLKO.1 vector) (Sigma) were used for silencing Akt (NM_009652), PP2a (NM_016891) genes in MEFs cells. For each shRNA were used a set of 5 clones validated to have at least 70% of knockdown.
NB4 cells were grown in DMEM supplemented with 10% FCS and infected with the adenovirus expressing mtAEQ.
For cell death induction cells were treated as indicated in the text with 1 mM H_2O_2, 15 μM MEN, 6 μM TN, 2 μM TG and 50 μM ETO in DMEM, supplemented with 10% FCS.
Apoptosis was determined by FACS analysis of cells stained with Annexin-V FITC/Propidium Iodide (BioVision).

Generation of erPML chimera and nuPML chimera expression vectors

ErPML chimera was addressed to the external surface of ER by fusing sequence from the yeast UBC6 (*1*) protein to the C-terminal end of the human PML isoform IV and I. PML protein was targeted to the nuclear matrix (nuPML) adding at the C-terminal end of the human PML isoform IV the sequence derived from the human glucocorticoid receptor NR3C1 (*2*).

Fura-2 measurements

Coverslips with cell monolayers were incubated at 37°C for 30 min in DMEM supplemented with 5 μM Fura2-AM (Molecular Probes). After a brief wash with KRB/Ca^{2+} (*3*) they were placed in an open Leyden chamber on the thermostatted stage of a Zeiss Axiovert 100 inverted microscope, equipped with a Sutter filterwheel and exposed to 340/380 wavelength light. Fluorescence data, collected with a Princeton Instruments back-illuminated camera, were calculated with Metafluor software (Universal Imaging) and expressed as emission ratios.

Aequorin measurements

Cells grown on 13 mm round glass coverslips at 50% confluence were transfected with the appropriate chimera cyt, mt and erAEQ (as previously described (*3*)) alone or together with expression constructs erPML, nuPML or m/p Akt.

All aequorin measurements were carried out in KRB. Agonists and other drugs were added to the same medium, as specified in the figure legends. The experiments were terminated by lysing the cells with 100 μM digitonin in a hypotonic Ca^{2+}-rich solution (10 mM $CaCl_2$ in H_2O), thus discharging the remaining aequorin pool. The light signal was collected and calibrated into $[Ca^{2+}]$ values, as previously described (*3*).
For NB4 cells, analysis of mitochondrial responses was made with an automated luminescence plate reader (MicrobetaJET, PerkinElmer, CA, USA).

Luciferase measurements
MEFs grown on 13 mm round glass coverslips at 50% confluence were transfected with mitochondrial luciferase (mtLuc). Measurements were performed 36 hr after transfection. Cell luminescence was measured in a luminometer as previously described (*4*). Cells were constantly perfused with a modified KRB containing 20 μM luciferin.

Sub-cellular Fractionation
Cells (10^9) were harvested, washed in phosphate- buffered saline medium, pelleted by centrifugation at 500 x g for 5 min, resuspended in homogenization buffer (0.25 M sucrose and 10 mM Hepes pH 7.4) and gently disrupted by dounce homogenisation. The homogenate was centrifuged twice at 600 x g for 5 min to remove cellular debris and nuclei, and the supernatant was centrifuged at 10.300 x g for 10 min to pellet crude mitochondria. The resultant supernatant was centrifuged at 100.000 x g for 1 h in a Beckman 70 Ti rotor at 4^0C to pellet microsomes, which were resuspended in homogenization buffer. The mitochondrial pellet, resuspended in isolation medium (250 mM mannitol, 5 mM Hepes (pH7.4), and 0.5 mM EGTA) was, layered on top of 8 ml of Percoll medium (225 mM mannitol, 25 mM Hepes (pH 7.4), 1 mM EGTA, and 30% Percoll (v/v)) in a 10-ml polycarbonate ultracentrifuge tube and centrifuged for 30 min at 95.000 x g. A dense band containing purified mitochondria, recovered approximately ¾ down the tube, was removed, diluted with isolation medium, washed twice by centrifugation at 6.300 x g for 10 min to remove the Percoll, and finally resuspended in isolation medium. MAM, removed from the Percoll gradient as a diffuse white band located above the mitochondria, were diluted in isolation medium and centrifuged at 6.300 x g for 10 min. The supernatant containing MAM was centrifuged at 100.000 x g for 1h in a Beckman 70 Ti rotor, and the resulting pellet was resuspended in the homogenization buffer (*5, 6*).
The quality of the preparation has been checked by western blot analysis using different markers for the fractions obtained.

- IP3R, as ER marker, should be present at about 20% in MAM fraction of than present in the ER.
- Voltage dependent anion channel (VDAC), as mitochondrial marker, should be present in Mc but must be enriched in Mp fraction. It should be also present in the MAM fraction.
- Tubulin, as cytosolic marker, should be absent in Mp, MAM and ER.
- Proliferating cell nuclear antigen (PCNA), as nuclear marker, should be absent in Mp and MAM.

Nuclei isolation (Based on Robert L. Ochs's protocol)
All steps are done at 4°C with buffers containing 1 mM PMSF (Sigma), Protease Inhibitor cocktail (Sigma), 2 mM Na_3VO_4 (Sigma), 2 mM NaF (Sigma), 1 mM DTT (Sigma). Cells are collected by centrifugation at 200 g for 5 min, washed once with ice-cold PBS, resuspended in 10 ml RSB-5 buffer (10 mM Tris-HCl, 10 mM NaCl, 5

mM Mg acetate, pH 7.4) per gram of cell pellet, and allowed to swell on ice for 30 min.
NP40 (Fluka) is added to a final concentratin of 0.3% and the mixture is homogenized with a Dounce homogenizer using 60-80 strokes. The efficiency of shearing cytoplasm from nuclei is monitored under a light microscopy, by staining with Trypan blue (Sigma) (stop when >90% of the cells are brust). An aliquot is saved as homogenate, and the remaining part is centrifugated at 1.200 g for 10 min to sediment crude nuclei. The supernatant is further centrifugated at 16.000 g for 30 min and this supernatant fraction is saved as cytoplasm. Nuclei are resuspended in 20 volumes of 0.88 M sucrose, 5 mM Mg acetate and centrifuged at 2.000 g for 20 min.
Nuclei are resuspended in RIPA buffer, incubate on ice for 30 minutes, vortexing every 5 minutes, and than centrifugate at 16.000 g for 10 min. Supernatant is saved as nuclear homogenate.

Western Blotting
30 μg of protein were separated by SDS-PAGE, transferred onto nitrocellulose membranes and probed using the following antibodies: anti-hPML (1:1000, Chemicon), anti-Pml (1:1000, Chemicon), anti-IP3R-3 (1:500, BD-Pharmingen), anti-βtubulin (1:1000, Santa Cruz), anti-PCNA (1:2000, Santa Cruz), anti-Laminin (1:1000, abcam), anti-panVDAC (1:5000, abcam), anti-αactin (1:2000, Santa Cruz), anti-pAkt (1:1000, Cell Signalling), anti-Akt (1:1000, Cell Signalling), anti-PP2a (1:1000, Cell Signalling), anti-FACL (1:500, Santa Cruz). Isotype matched, horseradish peroxidase conjugated secondary antibodies were used followed by detection by chemiluminescence (Perkin Elmer).

Immunolocalization of PML protein
MEFs were fixed with 3.7% formaldehyde in PBS for 20 min, washed three times with PBS and then incubated for 10 min in PBS supplemented with 50 mM NH_4Cl. Permeabilization of cell membranes was obtained with a 5 min incubation with 0.1% Triton X-100 in PBS, followed by a 1 h wash with 2% BSA in PBS. The cells were then incubated O/N at 37 °C in a wet chamber with the following antibodies: anti-PML (H-238) Santa Cruz (for erPML) or with the anti-Pml Chemicon (for endogenous Pml), anti-FACL Santa Cruz, anti-PP2a Cell Signalling, dilute 1:100 with 2% BSA in PBS. Staining was then carried out with Alexa 488 anti-rabbit for hPML (erPML), with Alexa 488 anti-mouse for Pml, with Alexa 543 anti-rabbit for PP2a and with Alexa 633 anti-goat for FACL secondary antibodies. After each antibody incubation the cells were washed four times with PBS. Fluorescence was then analyzed with a confocal microscope.

Immunoelectron microscopy
MEF cells are fixed with 2% paraformaldehyde and 0.2% glutaraldehyde in PBS, embedded in 12% gelatin, 2,3M sucrose and frozen in liquid nitrogen. Ultrathin cryo-sections, obtained by a Reichert-Jung Ultracut E with FC4E cryoattachment, were collected on copper-formvar-carbon-coated grids. Immunogold localization was revealed using the PML Chemicon antibody for endogenous mouse Pml and PML (H-238) Santa Cruz for erPML chimera and 10 nm proteinA-gold conjugated, according published protocols (*7, 8*). All samples were examined in a Philips CM10 or a FEI Tecnai 12G2 electron microscopes.

Blue-Native and SDS-PAGE 2D separation

Livers from *Pml*$^{+/+}$ and *Pml*$^{-/-}$ were gently homogenized in 1M aminocaproic acid, 50 mM Bis-Tris pH 7.0. The homogenate was centrifuged at 600 x g for 3 min to discard unbroken cells. To prepare "native" protein lysate, a mild neutral detergent n-dodecyl-β-D-maltoside in the final 1% concentration was used. The lysates were incubated on ice for 20 min and then centrifuged 20.000 x g for 15 minutes to remove unsolubilised material. Protein concentration in the liver lysates was determined according to the Bradford's method using Bio-Rad protein estimation kit. Afterwards, native lysates were combined with 5% Serva Blue G and 30 or 80 μg of protein was loaded and separated on a big dimensional (1 mm/16 cm/20 cm) 4-12% gradient acrylamide gel in the first dimension. As an internal standard – to see the quality of samples separation at the 1st dimension and to calibrate the BN gel (in kDa), sample containing 20 μg of rat hart mitochondria (RHM) was processed. Afterwards, the 1st dimension BN gel lines (corresponding to the separated individual samples), were equilibrated in a solution containing 2% SDS and 5 mM tributylphosphine (for reduction of cysteines) for 15 min and subsequently in a solution containing 2% SDS and 260 mM iodoacetamide (for the alkylation of cysteines) for another 15 min. Next, the 1st dimension BN gel lines were stacked over a 6 or 10 % SDS-PA gel, separated and transferred to the PVDF membrane. Then the membranes were immunoblotted against: IP3R3, Pml, Akt and PP2a. After hybridization with HRP peroxidase conjugated secondary antibody, the signal was revealed using ECL Plus Western blot detection reagent (Amersham Pharmacia Biotech).

Co-immunoprecipitation

Pml$^{+/+}$ and *Pml*$^{-/-}$ MEFs extracts were prepared using lysis buffer containing: 50 mM NaCl, 50 mM Tris-HCl pH 7.4, 0.1% NP-40 supplemented with 1 mM PMSF and proteases/phosphatases inhibitors. Protein extracts were pre-cleared with protein G/A beads (Pierce) than precipitated with IP3R3, Pml, Akt and PP2a antibodies overnight at 4°C (anti-IP3R3 BD-Pharmingen, anti-Pml Chemicon, anti-Akt Cell Signalling, anti-PP2a Cell Signalling). Protein G beads were added and rocked 5 hours at 4°C. Afterwards, beads were washed with 50 mM NaCl, 50 mM Tris-HCl pH 7.4, 0.1% NP-40 4°C. Samples were proceed by SDS-PAGE and analyzed by standard western blotting technique.

Statistical analysis of data

Statistical data are presented as mean ± S.D., significance was calculated by Student's t test, and correlation analysis was done with the SigmaPlot 5.0 software (SPSS Inc.).

Reference List

1. M. Yang, J. Ellenberg, J. S. Bonifacino, A. M. Weissman, *J Biol Chem* **272**, 1970 (Jan 17, 1997).
2. D. Picard, V. Kumar, P. Chambon, K. R. Yamamoto, *Cell Regul* **1**, 291 (Feb, 1990).
3. P. Pinton, A. Rimessi, A. Romagnoli, A. Prandini, R. Rizzuto, *Methods Cell Biol.* **80**, 297 (2007).

4. L. S. Jouaville, P. Pinton, C. Bastianutto, G. A. Rutter, R. Rizzuto, *Proc.Natl.Acad.Sci.U.S.A* **96**, 13807 (1999).
5. J. E. Vance, *Journal of Biological Chemistry* **265**, 7248 (1990).
6. M. R. Wieckowski, C. Giorgi, M. Lebiedzinska, J. Duszynski, P. Pinton, *Nat Protoc* **4**, 1582 (2009).
7. J. W. Slot, H. J. Geuze, S. Gigengack, G. E. Lienhard, D. E. James, *J Cell Biol* **113**, 123 (Apr, 1991).
8. S. Confalonieri, A. E. Salcini, C. Puri, C. Tacchetti, P. P. Di Fiore, *J Cell Biol* **150**, 905 (Aug 21, 2000).
9. A. Rimessi, C. Giorgi, P. Pinton, R. Rizzuto, *Biochim Biophys Acta* **1777**, 808 (Jul-Aug, 2008).
10. M. S. Song *et al.*, *Nature* **455**, 813 (Oct 9, 2008).
11. P. Pinton, C. Giorgi, R. Siviero, E. Zecchini, R. Rizzuto, *Oncogene* **27**, 6407 (Oct 27, 2008).

Legends to Supplementary Figures.

Supplementary Fig. 1 Mean ± SE of five independent experiments with $Pml^{+/+}$ and $Pml^{-/-}$ splenocytes treated for 12 h with 1 mM H_2O_2, 15 μM menadione (MEN), 6 μM tunicamycin (TN) and 2 μM thapsigargin (TG). The data show the percentage of cell death in the whole cell population negative for annexin-V-FITC and propidium iodide (PI) staining, analyzed by flow cytometry. Average values were obtained from three independent experiments.

Supplementary Fig. 2 The alteration in Ca^{2+} homeostasis in $Pml^{-/-}$ MEFs cells was associated with a partial reduction in agonist-dependent production of ATP. The traces show mitochondrial ATP concentration ($[ATP]_m$) changes elicited by mitochondrial Ca^{2+} increase in $Pml^{+/+}$ and $Pml^{-/-}$ MEFs perfused with 100 μM ATP agonist. Ca^{2+} stimulates the activity of three Ca^{2+}-sensitive dehydrogenases of the Krebs cycle (NAD^+-isocitrate-, 2-oxoglutarate-, and pyruvatedehydrogenase) thus enhancing the electron flow through the electron transport chain and increasing mitochondrial ATP production and, hence, ATP levels in the cytosol. This, in turn, allow the control of ATP-regulated cell processes (*9*). By using mitochondrial targeted luciferase construct (mtLuc), we dynamically monitored the effect of ATP agonist on $[ATP]_m$ as described in the methods section. mtLuc luminescence data are expressed as a percentage of the initial value. The traces are representative of four independent experiments.

Supplementary Fig. 3 (A) The agonist-dependent $[Ca^{2+}]_m$ response in HEK wt, before ($[Ca^{2+}]_m$ peak 5.47 ± 0.34 μM) and after PML depletion with RNA interference ($[Ca^{2+}]_m$ peak 2.23 ± 0.18 μM). Hek wt cells either expressing mtAEQ alone or mtAEQ and PML siRNA were challenged, where indicated, with ATP 100 μM. n=10 from three independent experiments and $p<0.01$.

Supplementary Fig. 4 APL is commonly treated with arsenic trioxide (As_2O_3), an agent causing a biphasic effect on PML nuclear bodies; short-term treatment promotes the selective proteasome-dependent degradation of PML-RARα fusion protein and recovery of nuclear bodies, whereas long exposure induces the degradation of PML and the consequent disassembly of the nuclear bodies (*10*).

(A) To mimic a model of APL in MEFs, $Pml^{+/-}$ MEFs were transduced with a retrovirus expressing a fusion protein between PML and retinoic acid receptor α, RARα (PML-RARα). Notably, $Pml^{+/-}$ MEFs exhibited a mitochondrial Ca^{2+} response

to agonist stimulation in-between to those observed in *Pml*$^{+/+}$ and *Pml*$^{-/-}$ MEFs. *Pml*$^{+/+}$: $[Ca^{2+}]_m$ peak 115 ± 14 μM. *Pml*$^{-/-}$: peak 68 ± 9 μM. *Pml*$^{+/-}$: $[Ca^{2+}]_m$ peak 85 ± 17 μM. n=12 from three independent experiments and $p<0.05$. PML-RARα expression induced a reduced mitochondrial Ca^{2+} response to agonist stimulation to values comparable to those in Pml$^{-/-}$. *Pml*$^{+/-}$ expressing PML-RARα: $[Ca^{2+}]_m$ peak 79 ± 13 μM. n=15 from three independent experiments

Treatment with 1 μM As_2O_3 for 1 h restored the mitochondrial Ca^{2+} response to agonist stimulation in *Pml*$^{+/-}$ expressing PML-RARα: $[Ca^{2+}]_m$ peak 105 ± 10 μM. n=15 from three independent experiments and $p<0.05$. On the contrary, treatment with As_2O_3 did not affect mitochondrial Ca^{2+} response in *Pml*$^{+/+}$ (peak108 ± 11 μM), *Pml*$^{-/-}$ (peak 62 ± 13 μM) and *Pml*$^{+/-}$ (peak 83 ± 19 μM) cells (inset). n=6 from three independent experiments.

(B) Analysis of $[Ca^{2+}]_m$ responses in NB4 cells, a human APL cell line encoding the PML-RARα fusion protein, after apoptotic stimulation with 2 mM H_2O_2. Treatment with 1 μM As_2O_3 for 1 h induced an increased mitochondrial Ca^{2+} response (NB4: $[Ca^{2+}]_m$ peak 2.15 ± 0.12 μM, NB4 + As_2O_3: $[Ca^{2+}]_m$ peak 2.89 ± 0.08 μM) due to the PML-RARα degradation (*10*). n=6 from two independent experiments and $p<0.05$.

Supplementary Fig. 5 (A) Immunofluorescence of *Pml*$^{-/-}$ MEFs expressing erPML stained with: the anti-PML antibody, the anti-FACL antibody (as MAM marker) and Hoechst (as nuclear marker). The immunocytochemical staining pattern of erPML and FACL shows an extensive overlap. **(B)** Immunogold labeling of PML to the Rough ER (r), mitochondria (m) and MAM (arrowheads). Clusters of gold particles (15 nm) are localized associated to ER cisternae and occasionally to mitochondria (left panel). Morphologically identified MAM often demonstrate labeling associated to contact sites. ER/mitochondria contacts (right panel). BAR = a: 288 nm; b: 385 nm. **(C)** Immunoblot of PML after sub-fractionation in *Pml*$^{-/-}$ MEFs stably expressing erPML. After nuclei isolation, erPML was almost absent in the nucleus fraction and was enriched in the cytosolic fraction (left panel). However, when the latter was ultra-centrifuged to obtain a pure ER fraction separated from cytosolic fraction, Pml was mainly enriched in the ER fraction (right panel).

Supplementary Fig. 6 erPML chimera generated with PML isoform I re-establishes the agonist-dependent $[Ca^{2+}]_m$ response in *Pml*$^{-/-}$ MEFs ($[Ca^{2+}]_m$ peak 128 ± 16 μM) to values comparable to those obtained with erPML generated with PML isoform IV (shown in Fig. 3B). n=12 from three independent experiments.

Supplementary Fig. 7 (A) Percentage of cell death induced by transfection of erPML in *Pml*$^{-/-}$ MEFs treated with 1 mM H_2O_2, 15 μM menadione (MEN), 6 μM tunicamycin (TN), 2 μM thapsigargin (TG) or 50 μM etoposide (ETO). Cell viability was evaluated after a 16 h treatment. The data show the percentage of cell death in the whole cell population negative for annexin-V-FITC and propidium iodide (PI) staining, analyzed by flow cytometry. Average values were obtained from three independent experiments. **(B)** Analysis of $[Ca^{2+}]_m$ during 100 μM ETO stimulation in *Pml*$^{+/+}$ and *Pml*$^{-/-}$ MEFs. n=7 from two independent experiments.

Supplementary Fig. 8 (A) Schematic map of the chimeric PML targeted to the nucleus and immunofluorescence image of *Pml*$^{-/-}$ MEFs expressing nuPML and stained with the anti-PML antibody **(B)** nuPML did not re-establishes the agonist-dependent $[Ca^{2+}]_m$ response in *Pml*$^{-/-}$ MEFs ($[Ca^{2+}]_m$ peak 83 ± 9 μM) compared to the effects of erPML (Fig. 3B and 3D). n=8 from three independent experiments. **(C)** nuPML did not re-establishes sensitivity to Ca^{2+}-dependent apoptotic stimuli but restored the etoposide (ETO)-dependent cell death. Representative microscopic fields, from three independent experiments, of *Pml*$^{-/-}$ MEFs and *Pml*$^{-/-}$ expressing nuPML

before and after treatment with 1 mM H_2O_2, 15 μM menadione (MEN) or 50 μM ETO for 16 h.

Supplementary Fig. 9 Original western blot membranes of data presented in Fig. 4A.

Supplementary Fig. 10 Co-immunoprecipitation of IP3R3 using Pml, Akt and PP2a as bait in *Pml*$^{+/+}$ MEFs.

Supplementary Fig. 11 Densitometric analysis of the data (three independent experiments of the Western blot of p-IP3R3, pAkt and PP2a levels) presented in Fig. 4A.

Supplementary Fig. 12 Schematic model of Pml effects on type 3 IP3R-dependent apoptosis. In *Pml*$^{+/+}$ MEFs, PML induces the interaction between Akt and PP2a. Thus, the phosphorylation state of the IP3R3 is controlled. On the contrary, in *Pml*$^{-/-}$ the PP2a dephosphorylation of Akt is inhibited, and thus pAkt accumulates. As a consequence, the higher amount of IP3R3 is phosphorylated, the Ca^{2+} released after apoptotic stimulation is reduced and apoptosis is inhibited.

Supplementary Fig. 13 High resolution Blue-Native and SDS-PAGE 2D separation of Pml, IP3R3, PP2a and Akt containing complexes from the liver native extracts of *Pml*$^{+/+}$ **(A, A')** and *Pml*$^{-/-}$ **(B, B')** mice. Pml was present in varying amounts in complexes of a wide of molecular size range.

2D separation was performed as described in Methods and PVDF membranes were immunobloted against IP3R3, Pml, PP2a and Akt. The BN-PAGE was calibrated based on the location of the mitochondrial respiratory chain complexes isolated from rat heart mitochondria (RHM), electrophoretically separated simultaneously with the native liver extracts on BN-PAGE (panel C). In the upper left inset (A'), a lower amount of protein loaded on BN gel exhibits a more clear and background-less immunoblot of Pml protein present in varying amounts in complexes of a wide molecular size range. At the same time, a slight signal of IP3R3 in the high molecular weight complexes is visible (inserts A' and B'). Due to the low amount of protein separated on BN PAGE both PP2a and Akt were not detectable in these conditions. To visualize the complexes formed by all these four proteins, higher amounts of native extracts were used and separated on a 6 % acrylamide gel in the second dimension. We found that in *Pml*$^{+/+}$ native extracts, Akt and PP2a are present in the same area of the high molecular weight complexes where Pml and IP3R3 were detected (see arrows, panel A). In contrast, in *Pml*$^{-/-}$ native extracts, PP2a is not present in regions where IP3R3 and Akt are participating in the formation of high molecular weight complexes (see arrows, panel B).

Supplementary Fig. 14 Merged images of pairs of following co-localization analyzed by immunofluorescence presented in Fig. 4B: Pml (green) + PP2a (red), Pml (green) + FACL (blue), PP2a (red) + FACL (blue).

Supplementary Fig. 15 Effects of okadaic acid (OA) (1 μM, 1 hour) on agonist-dependent $[Ca^{2+}]_m$ responses in *Pml*$^{+/+}$ MEFs **(A,** peak 92 ± 21 μM vs 128 ± 33 μM in control cells, $p<0.01$); *Pml*$^{-/-}$ MEFs **(B,** peak 73 ± 22 μM vs 78 ± 14 μM in control cells) and *Pml*$^{-\backslash-}$ MEFs expressing erPML **(C,** peak 102 ± 13 μM vs. 135 ± 17 μM in control cells, $p<0.05$**)**. Effects of LY294002 (5 μM, 30 min) on agonist-dependent $[Ca^{2+}]_m$ responses in *Pml*$^{+/+}$ **(D,** peak 126 ± 16 μM vs 128 ± 33 μM in control cells**)**, *Pml*$^{-/-}$ **(E,** peak 112 ± 15 μM vs 78 ± 14 μM in control cells, $p<0.01$**)** and *Pml*$^{-\backslash-}$ expressing erPML MEFs **(F,** peak 124 ± 13 μM vs 132 ± 18 μM in control cells). For all these experiments n ≥15 of at least five independent experiments.

Supplementary Fig. 16 Schematic model of okadaic acid (OA) effects on *Pml*$^{+/+}$ and *Pml*$^{-/-}$.

Supplementary Fig. 17 Schematic model of LY294002 effects on *Pml*$^{+/+}$ and *Pml*$^{-/-}$.

Supplementary Fig. 18 Representative microscopic fields of MEFs, *Pml*$^{+/+}$, *Pml*$^{-/-}$ and *Pml*$^{-/-}$ expressing erPML, control (ctr) and treated first with okadaic acid (OA) (1 μM, 1 h) or LY294002 (5 μM, 30 min) and then 1 mM H_2O_2 or 15 μM menadione (MEN) (16 h).

Supplementary Fig. 19 Effects of Akt and PP2a silencing (inset) on agonist-dependent $[Ca^{2+}]_m$ responses in MEFs *Pml*$^{+/+}$ **(A)** [124 ± 30 μM in control cells vs peak 119 ± 21 μM (Akt shRNA) and peak 92 ± 18 μM (PP2a shRNA), $p<0.05$] and *Pml*$^{-/-}$ **(B)** [75 ± 28 μM in control cells vs peak 104 ± 23 μM (Akt shRNA), $p<0.05$ and peak 68 ± 19 μM (PP2a shRNA)]**. (C)** Analysis of $[Ca^{2+}]_m$ response in MEFs *Pml*$^{+/+}$ and *Pml*$^{-/-}$ overexpressing the constitutively active myristoylated/palmitylated AKT1 (m/p Akt). *Pml*$^{+/+}$: m/p Akt peak 89 ± 13 μM vs 120 ± 28 μM in control cells, $p<0.05$. *Pml*$^{-/-}$: m/p Akt peak 99 ± 21 μM vs 92 ± 10 μM in control cells. For all these experiments n ≥15 of at least five independent experiments.

Supplementary Fig. 20 Schematic model of Pml effects on Ca^{2+} homeostasis. Pml localized at the ER and MAM, to the outer surface of the ER, interacts with IP3R3, Akt and PP2a. This interaction is fundamental for the modulation of IP3R3-phosphorylation and in turn for IP3R dependent Ca^{2+} release.

The consequences of loss of Pml function are strikingly similar, both in magnitude and outcome, to those observed in cells overexpressing the Bcl-2 protein or depleted of Bax and Bak proteins in which increased IP3R phosphorylation also causes a reduction in the transfer of Ca^{2+} from ER to mitochondria (*11*).

Giorgi et al. Fig.S1

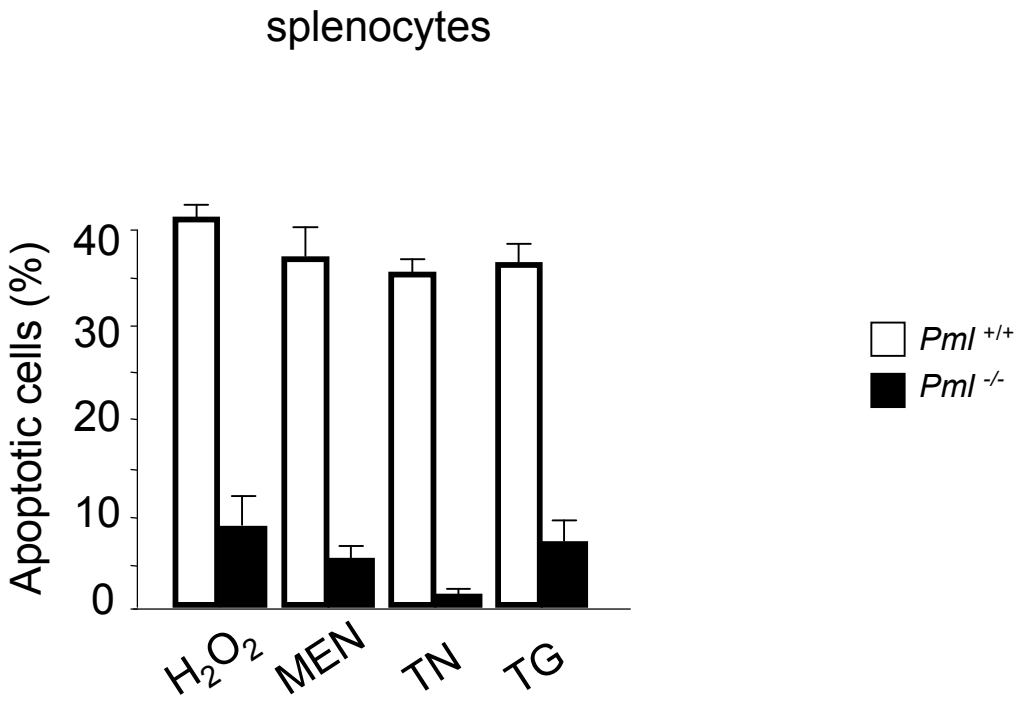

Giorgi et al. Fig.S2

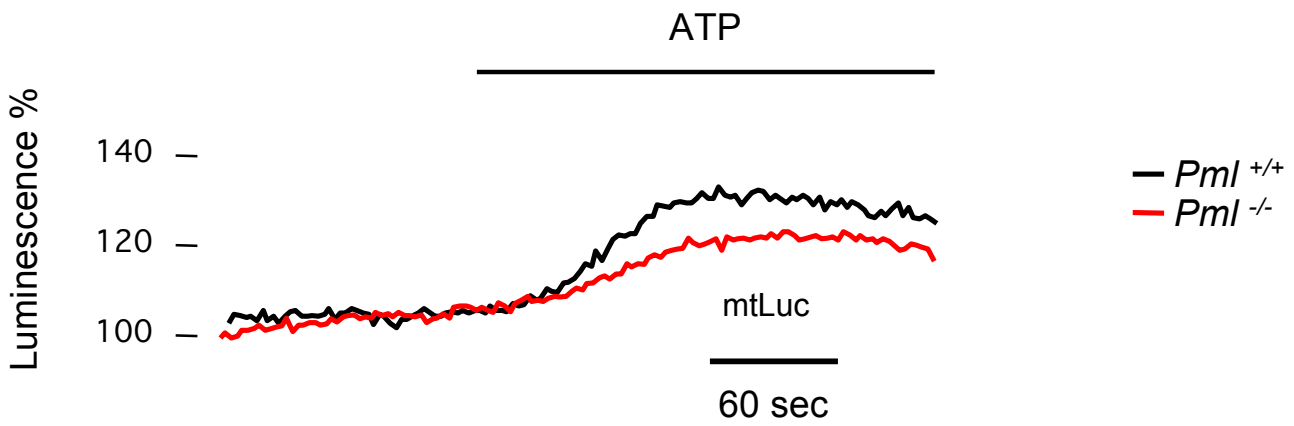

Giorgi et al. Fig.S3

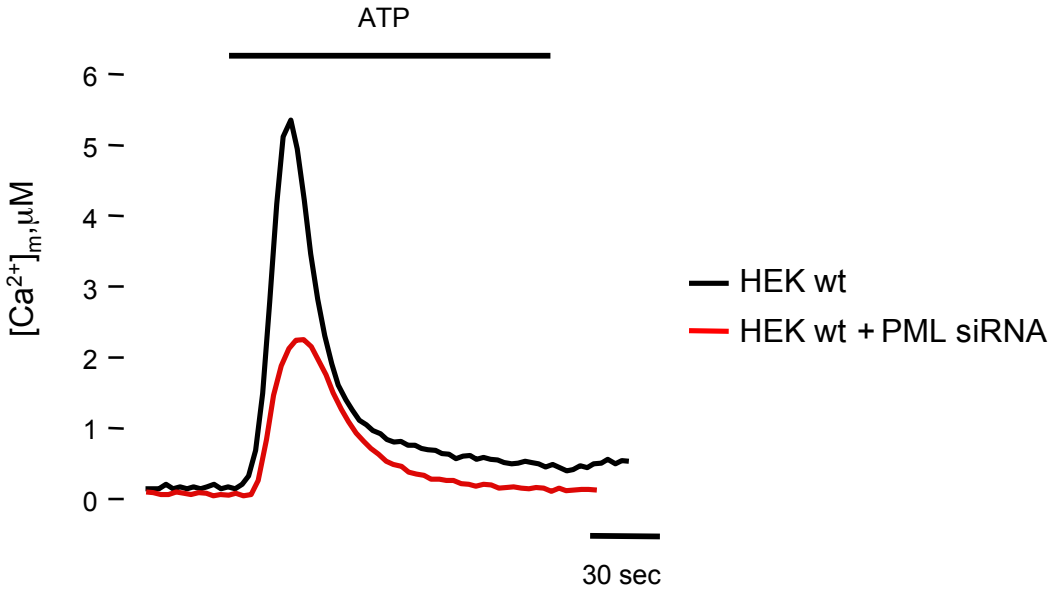

Giorgi et al. Fig.S4

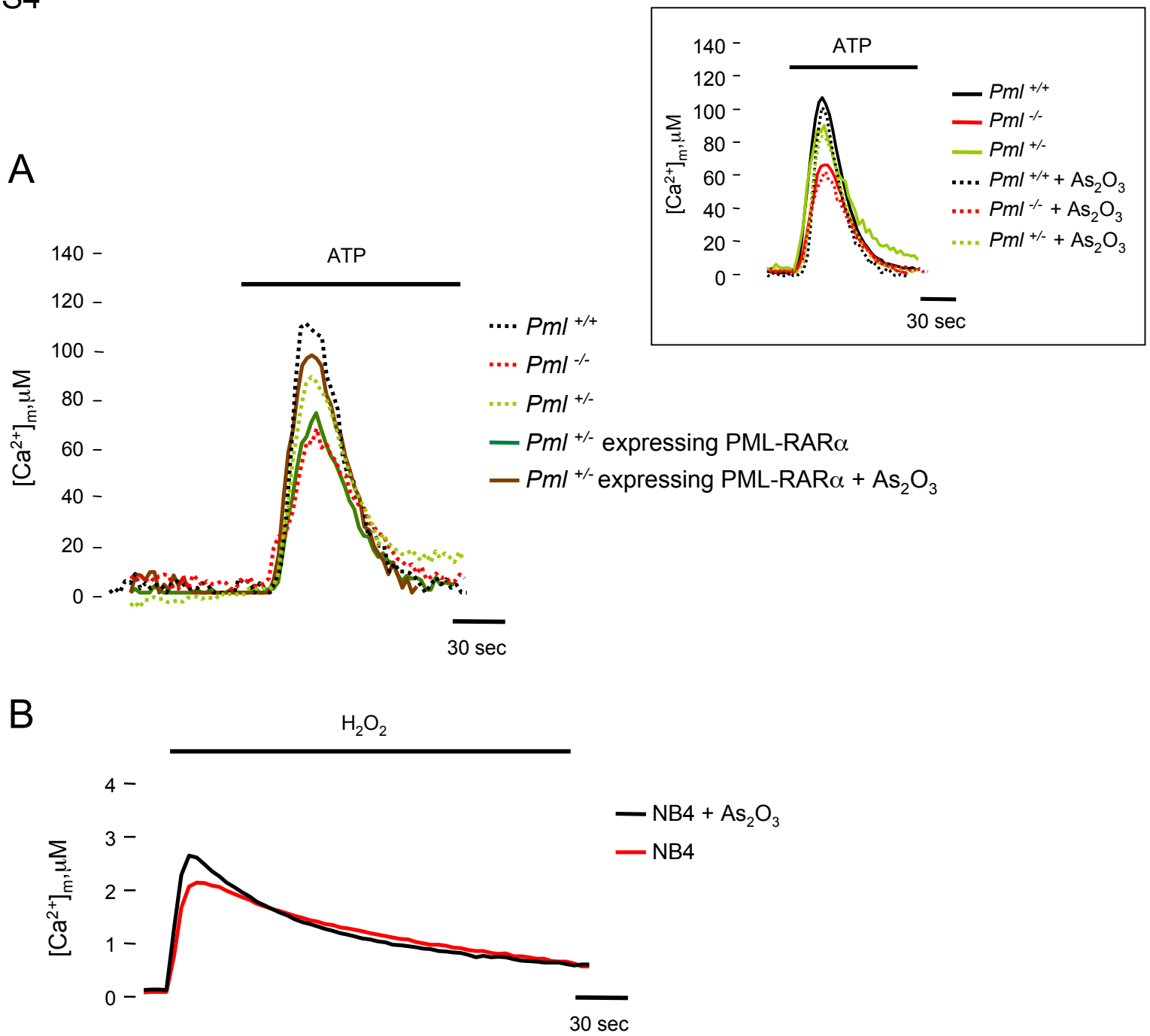

Giorgi et al. Fig.S5

A

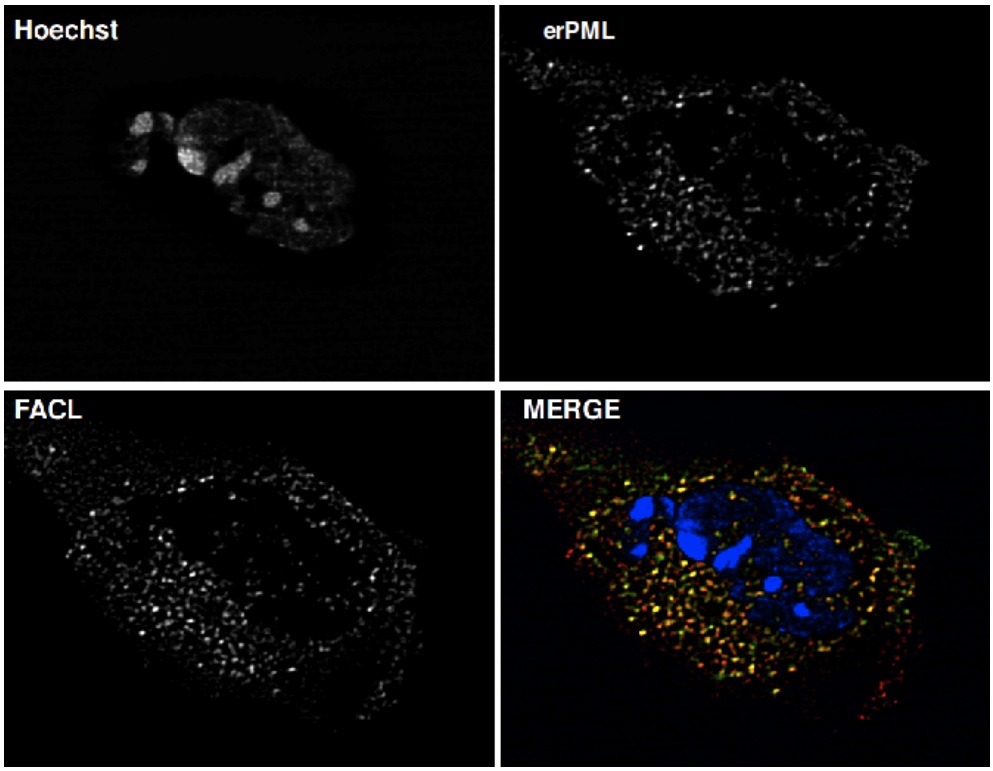

B

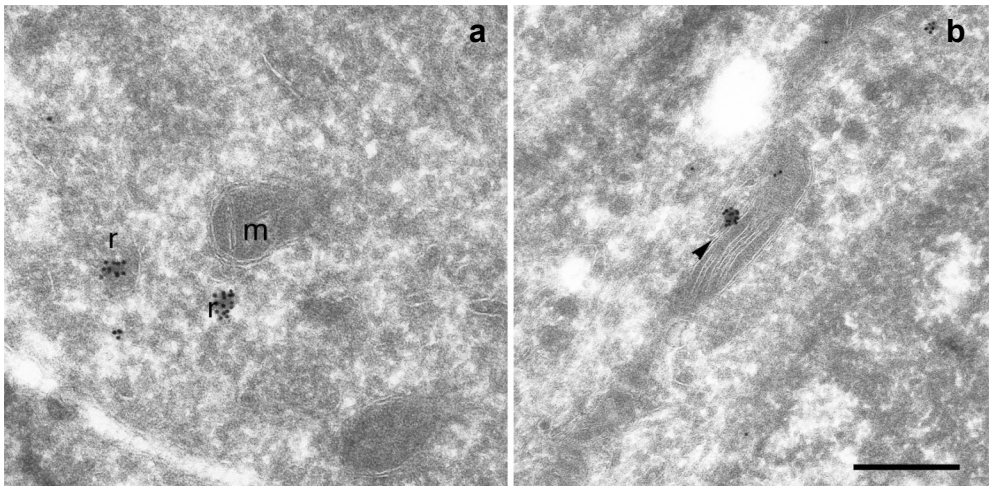

C

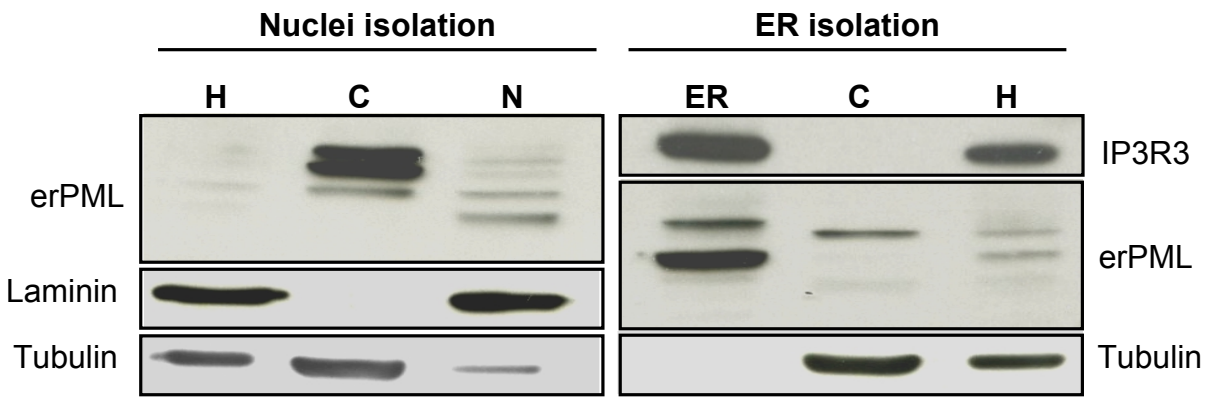

Giorgi et al. Fig.S6

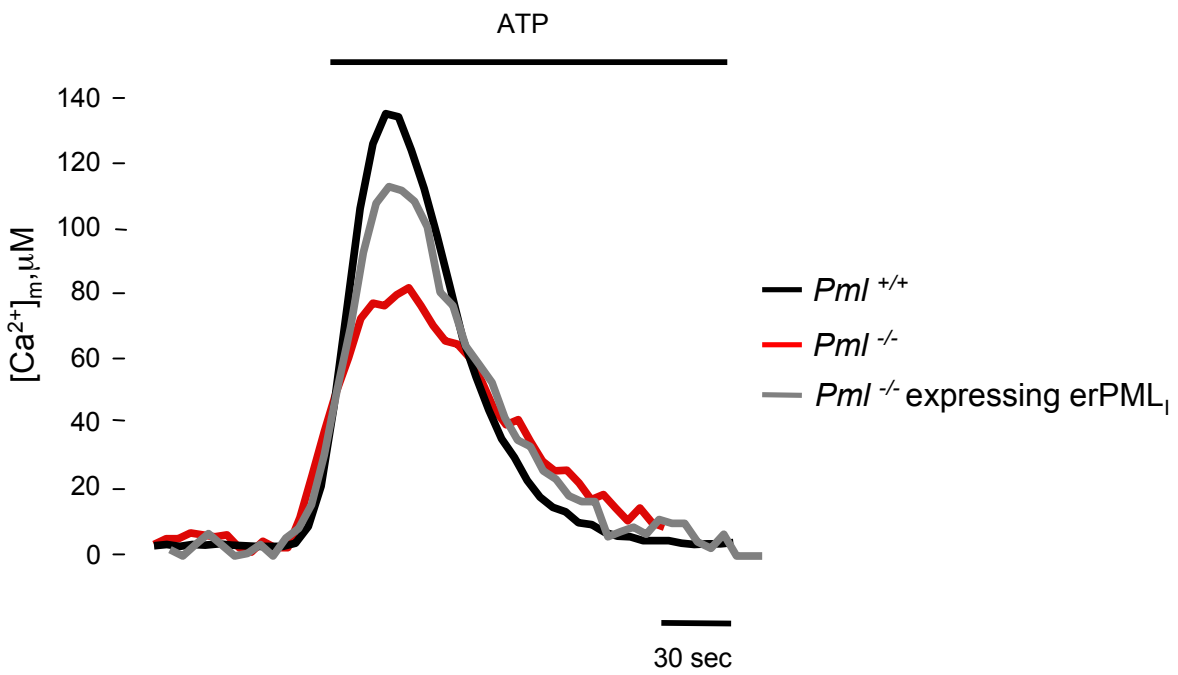

Giorgi et al. Fig.S7

A

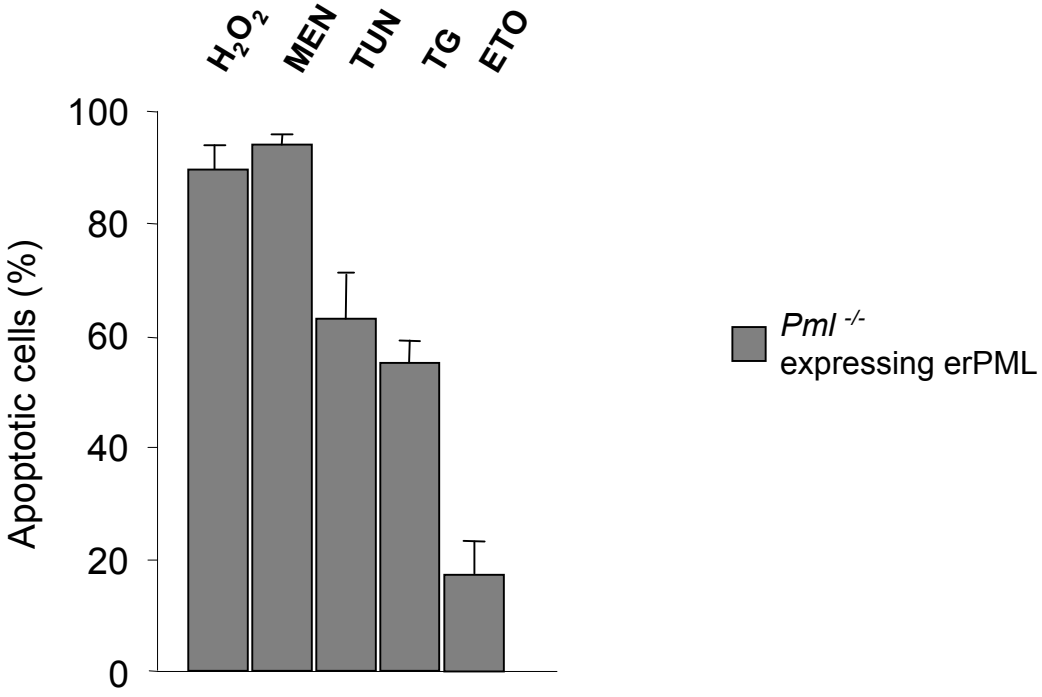

B

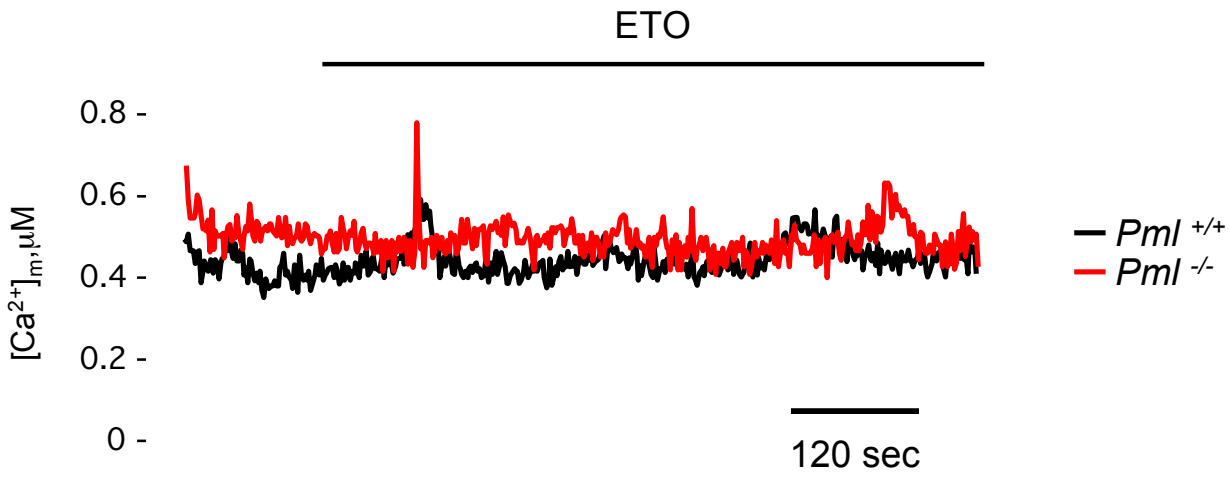

Giorgi et al. Fig.S8

A

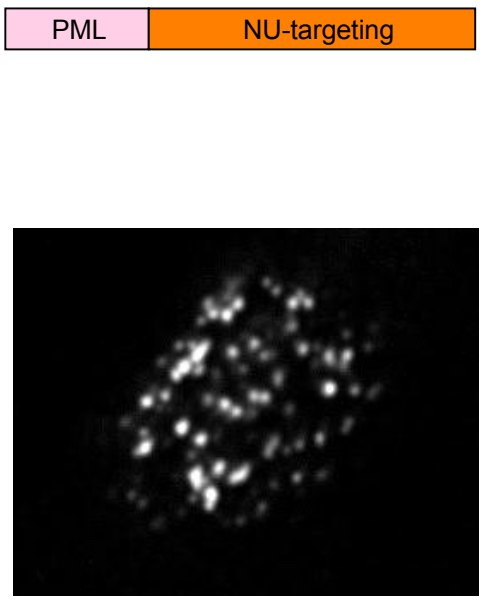

B

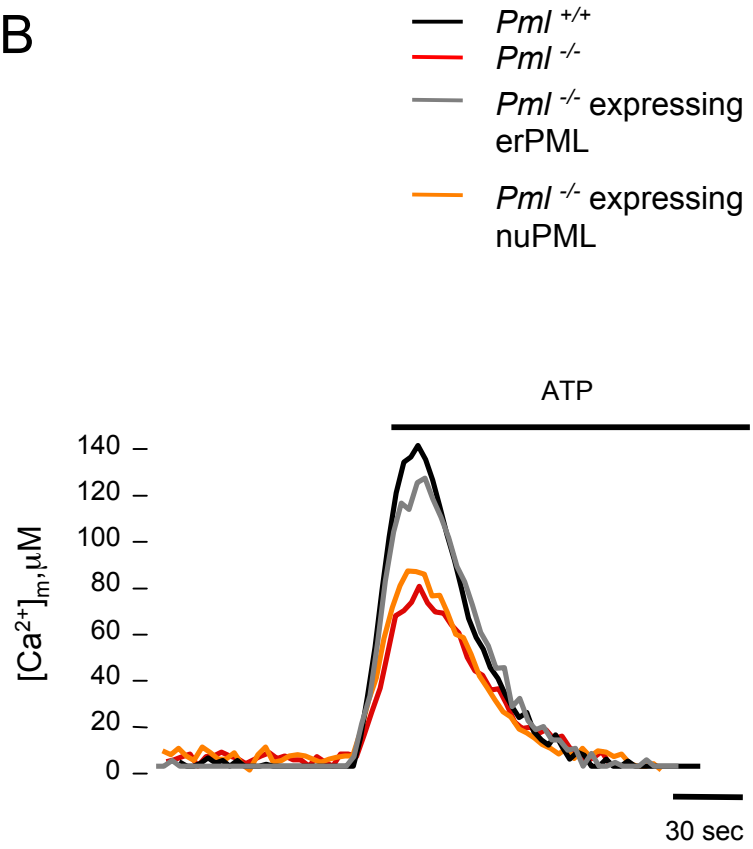

C

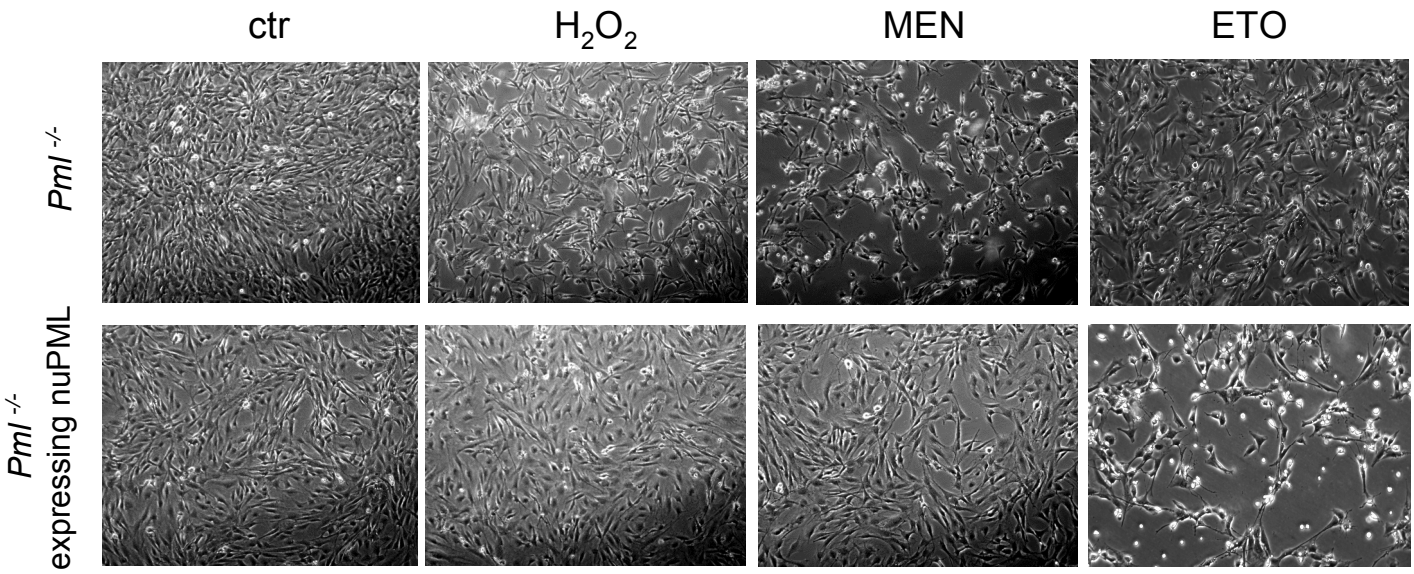

Giorgi et al. Fig.S9

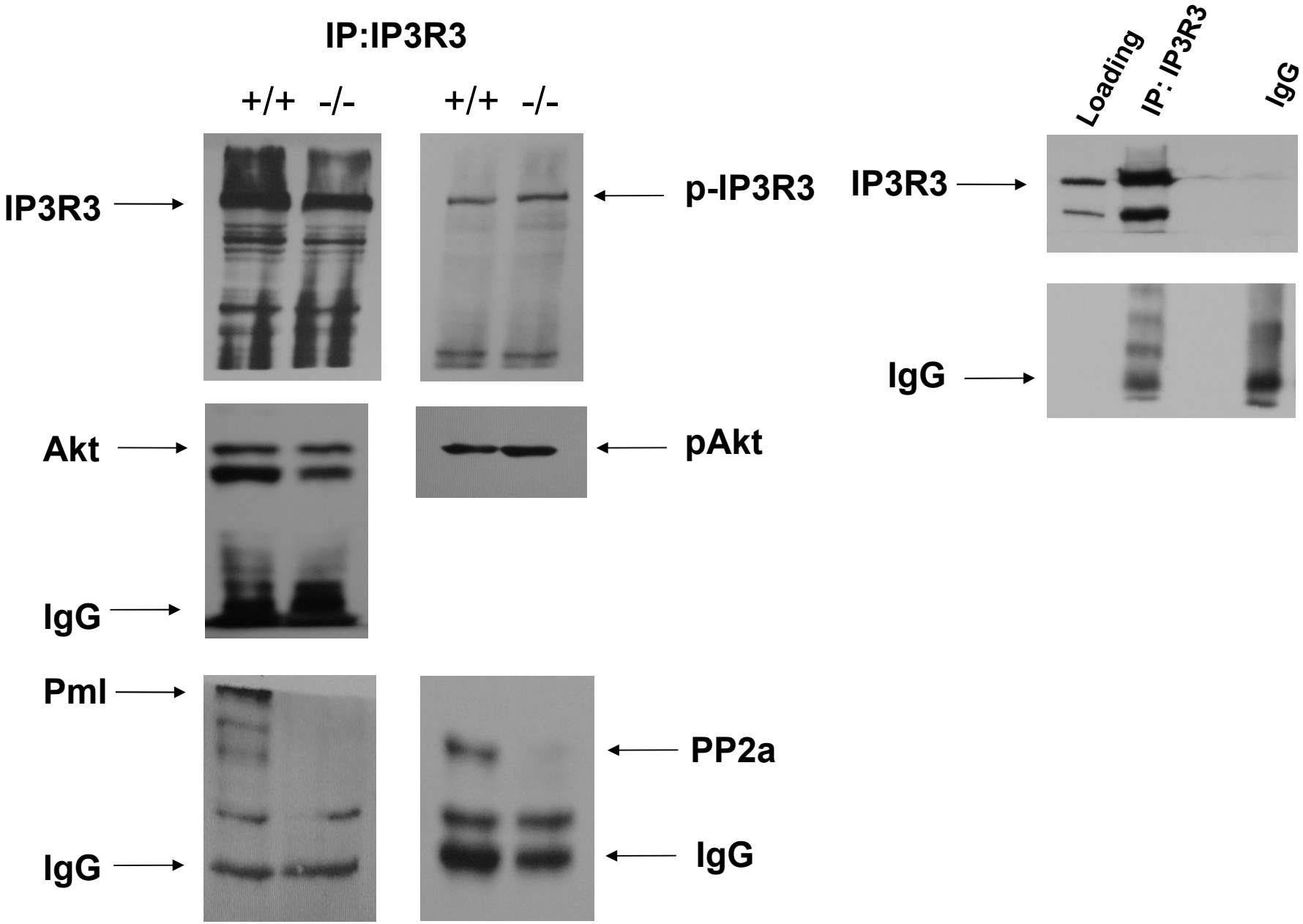

Giorgi et al. Fig.S10

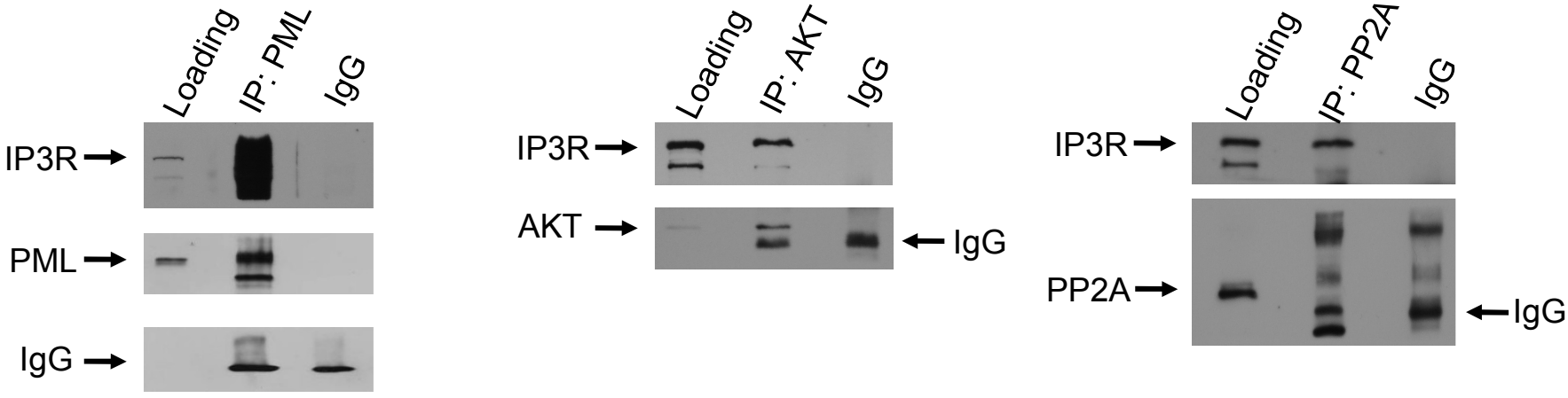

Giorgi et al. Fig.S11

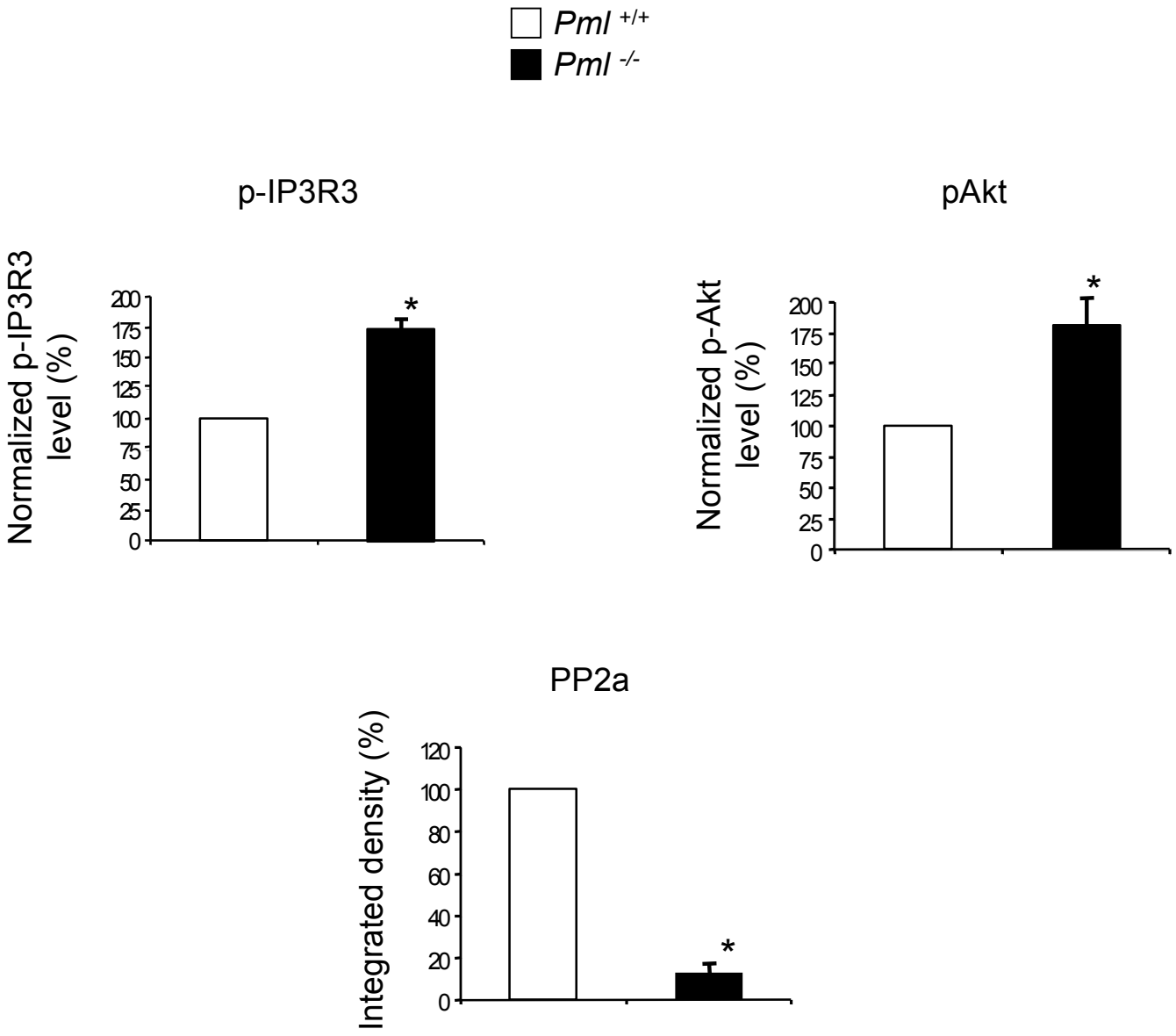

Giorgi et al. Fig.S12

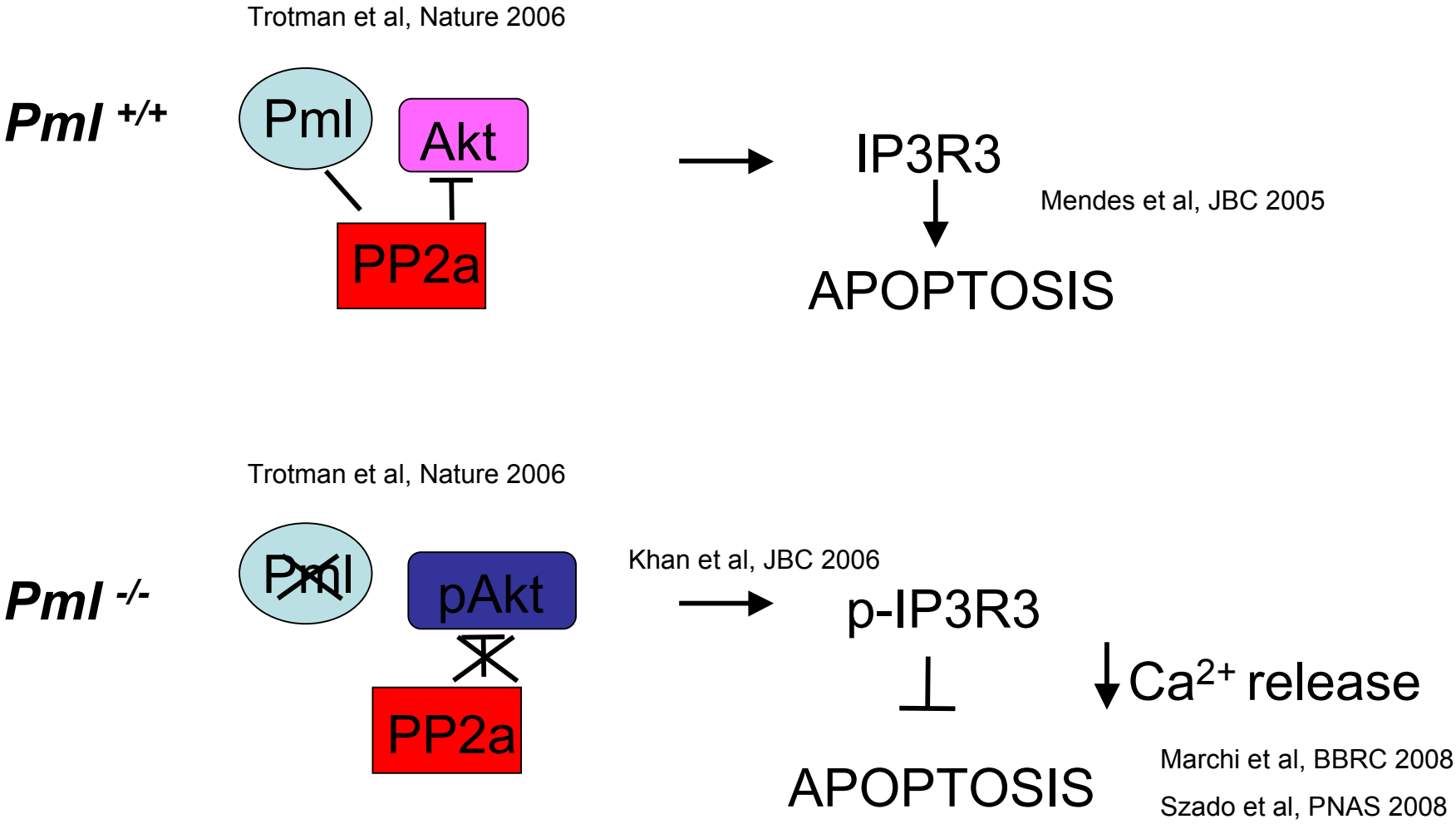

Giorgi et al. Fig.S13

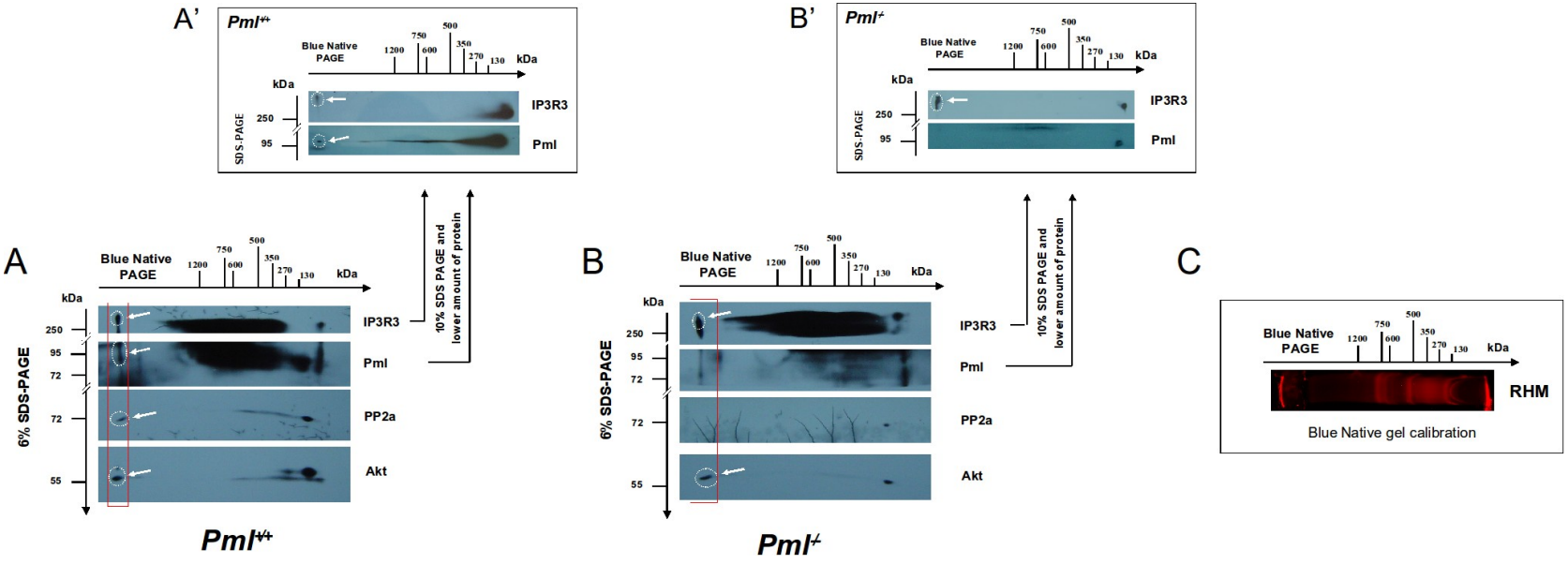

Giorgi et al. Fig.S14

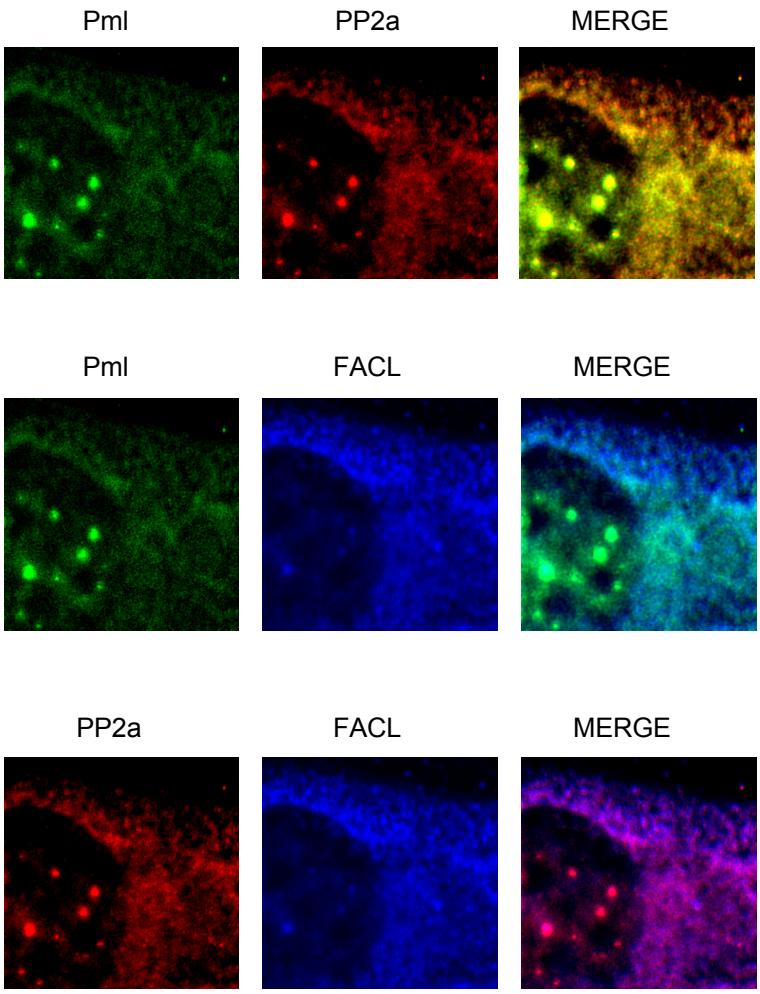

Giorgi et al. Fig.S15

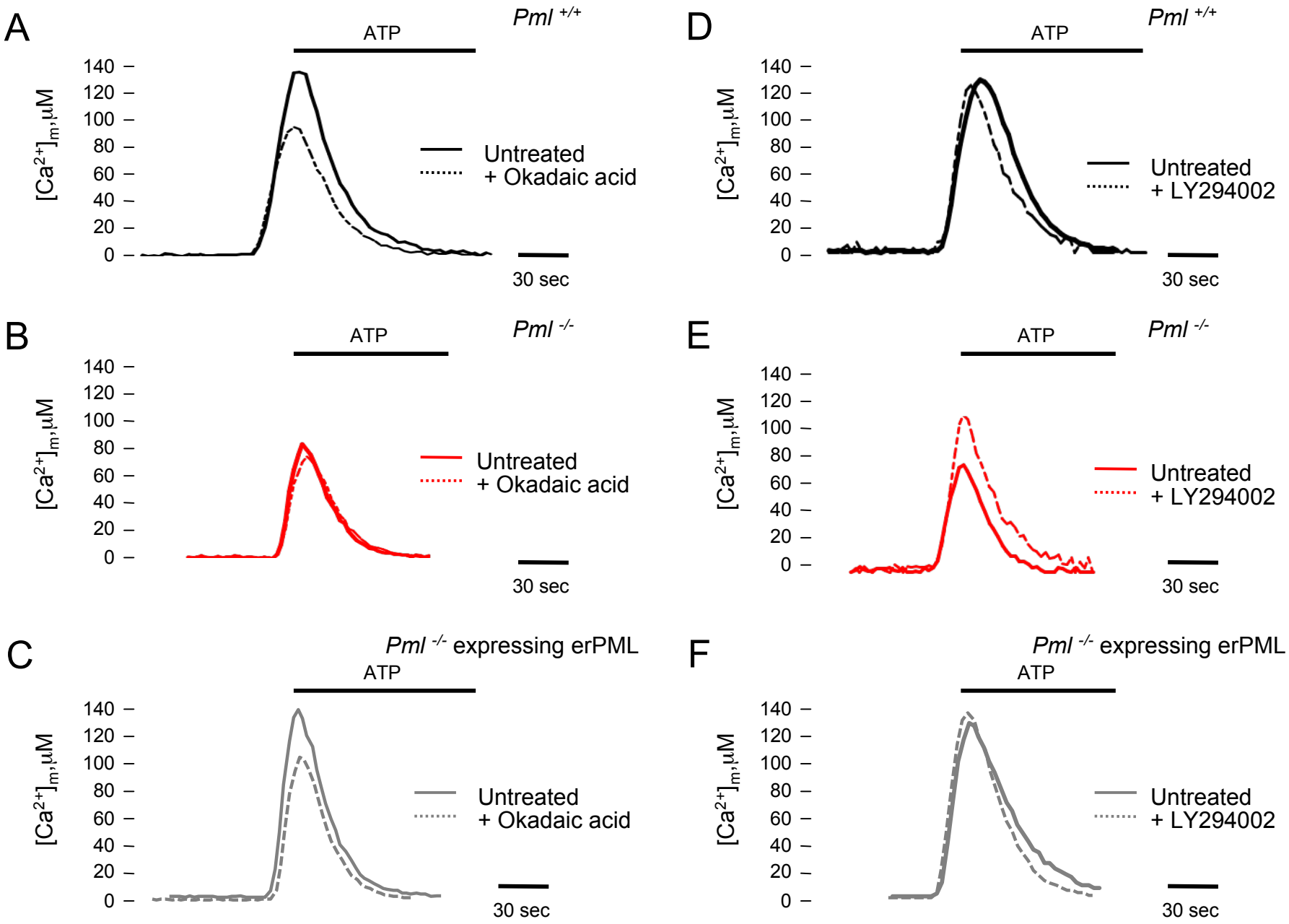

Giorgi et al. Fig.S16

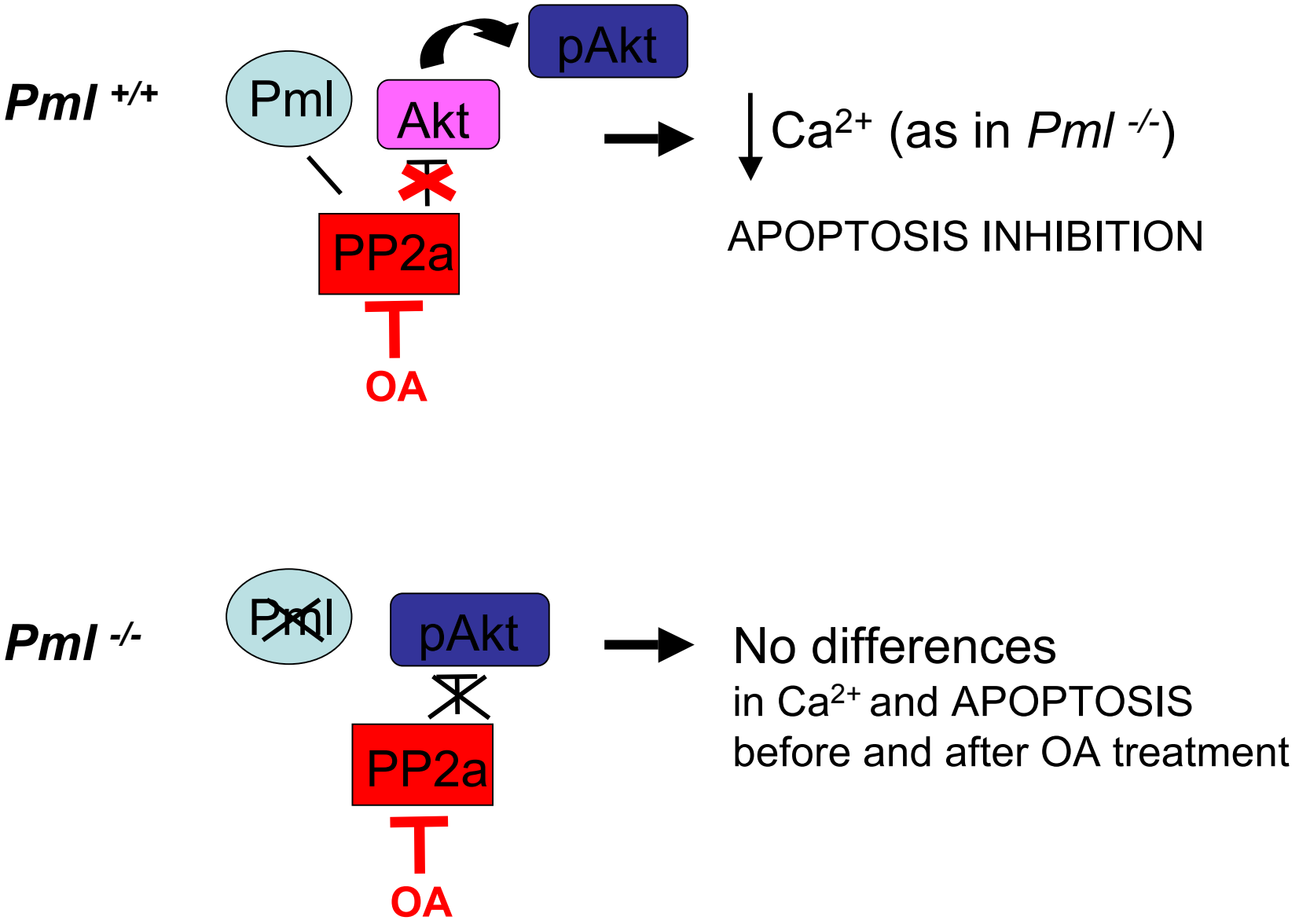

Giorgi et al. Fig.S17

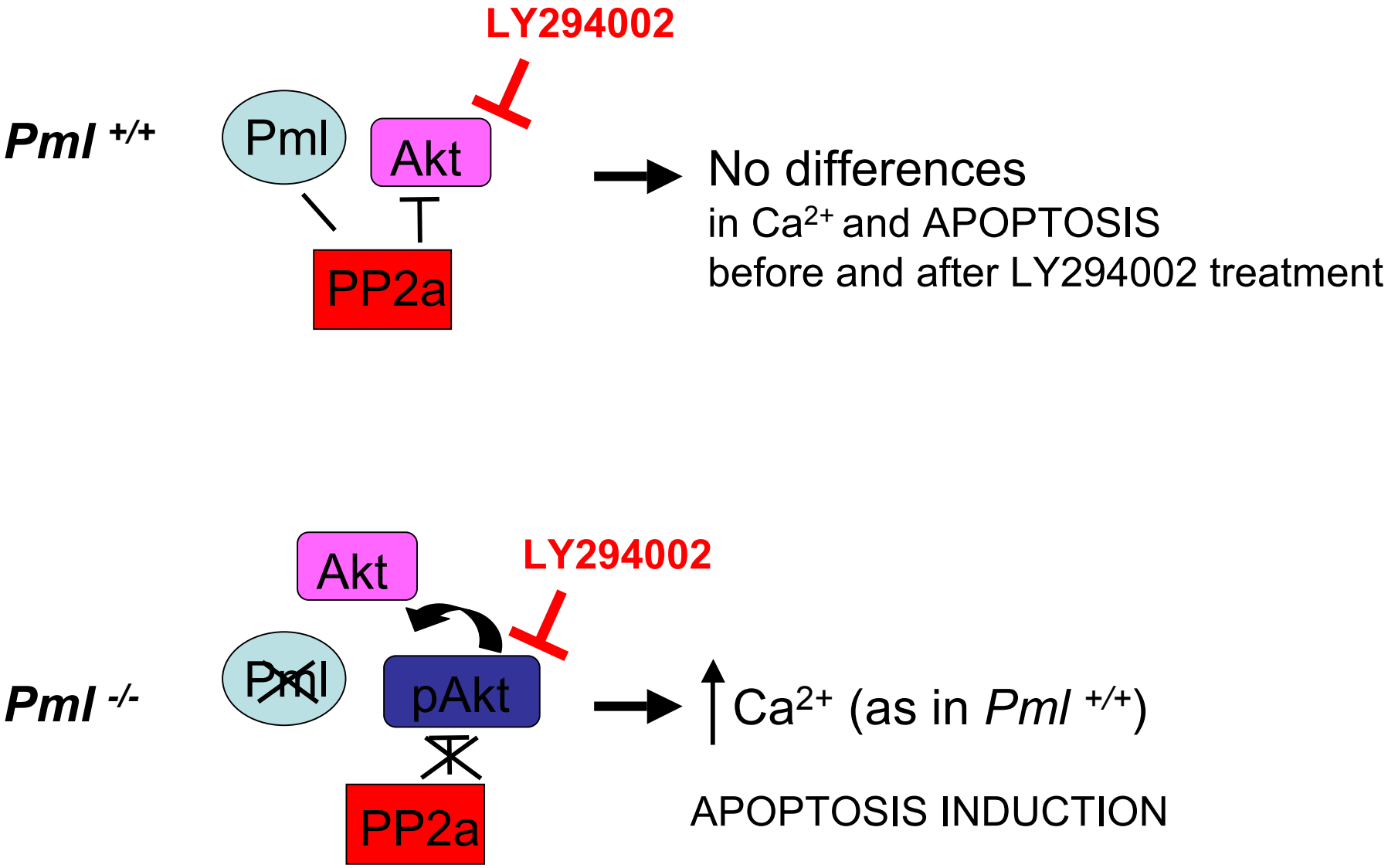

Giorgi et al. Fig.S18

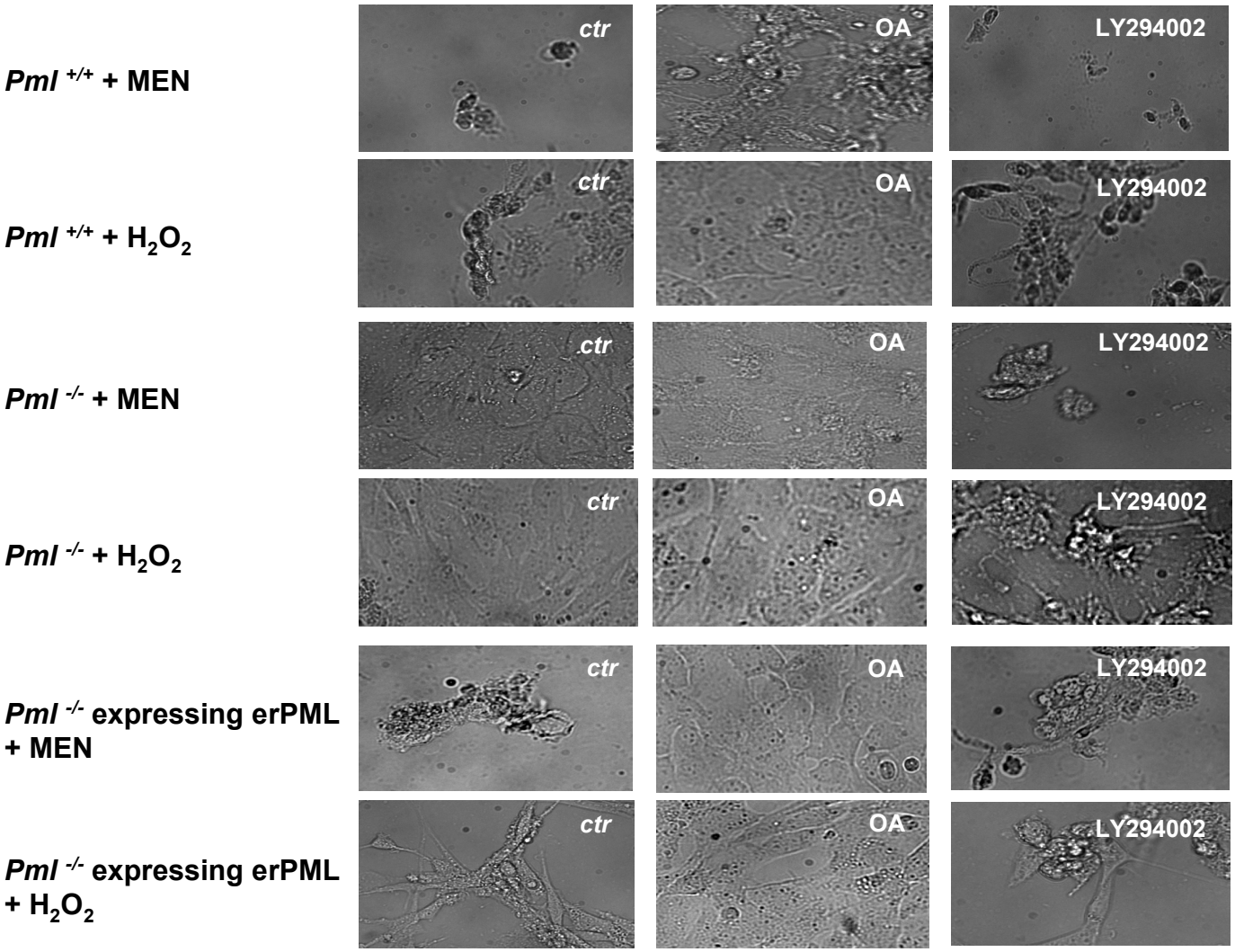

Giorgi et al. Fig.S19

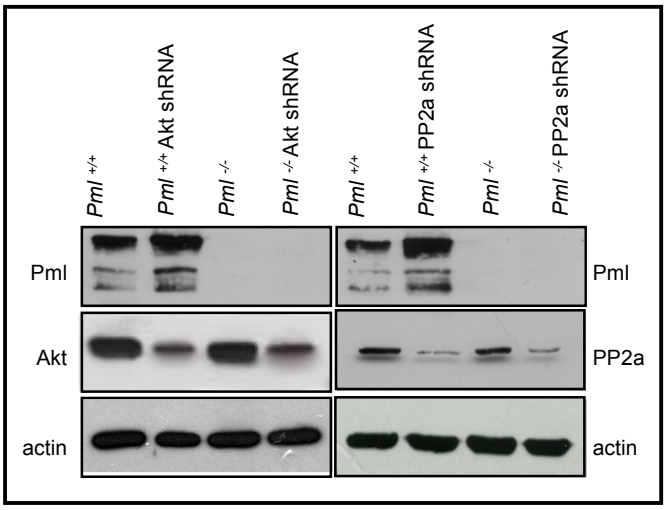

— *Pml* $^{+/+}$
···· *Pml* $^{+/+}$ Akt shRNA
- - *Pml* $^{+/+}$ PP2a shRNA

— *Pml* $^{-/-}$
···· *Pml* $^{-/-}$ Akt shRNA
- - *Pml* $^{-/-}$ PP2a shRNA

A

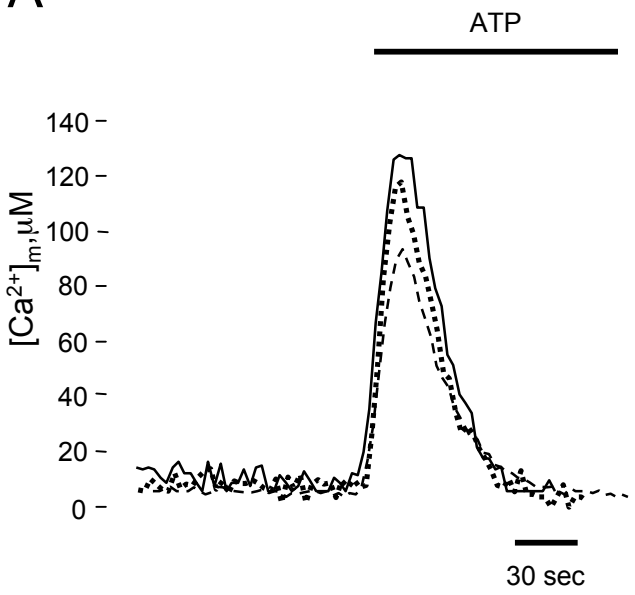

B

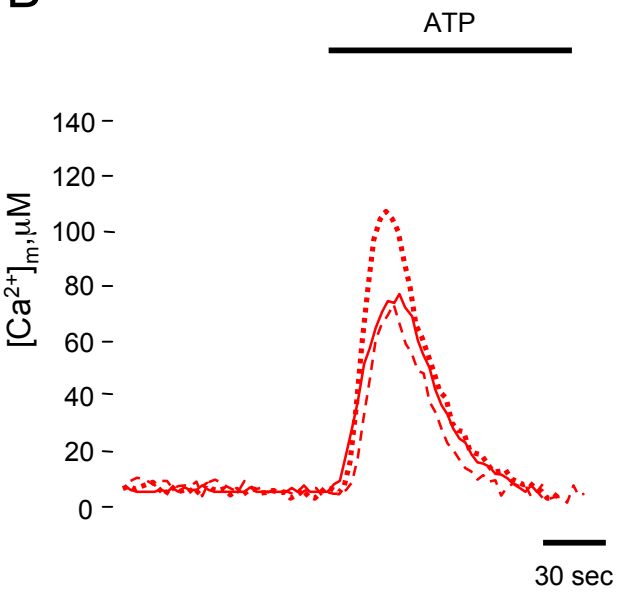

C

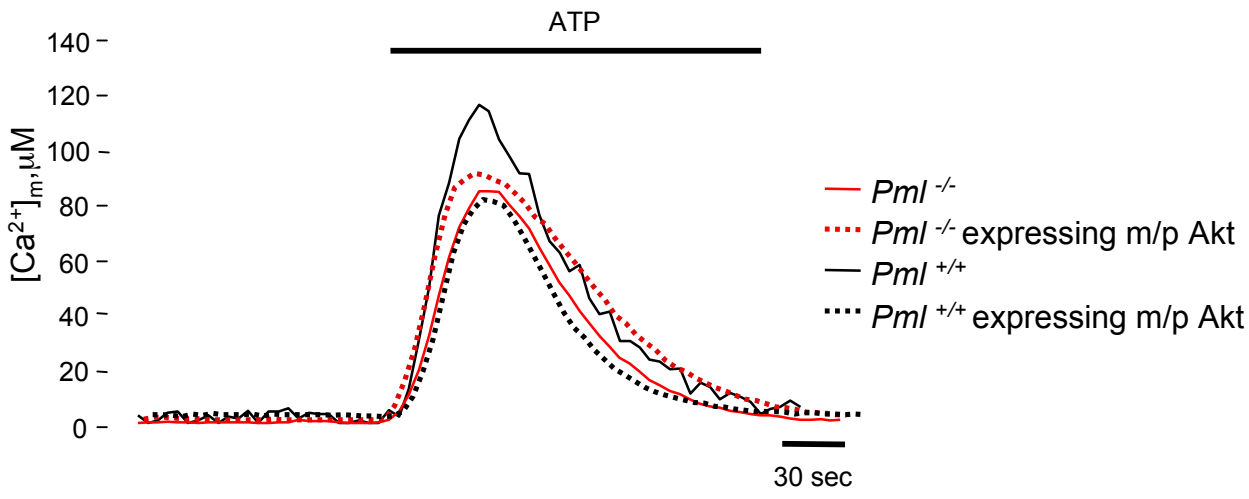

Giorgi et al. Fig.S20

Pml $^{+/+}$

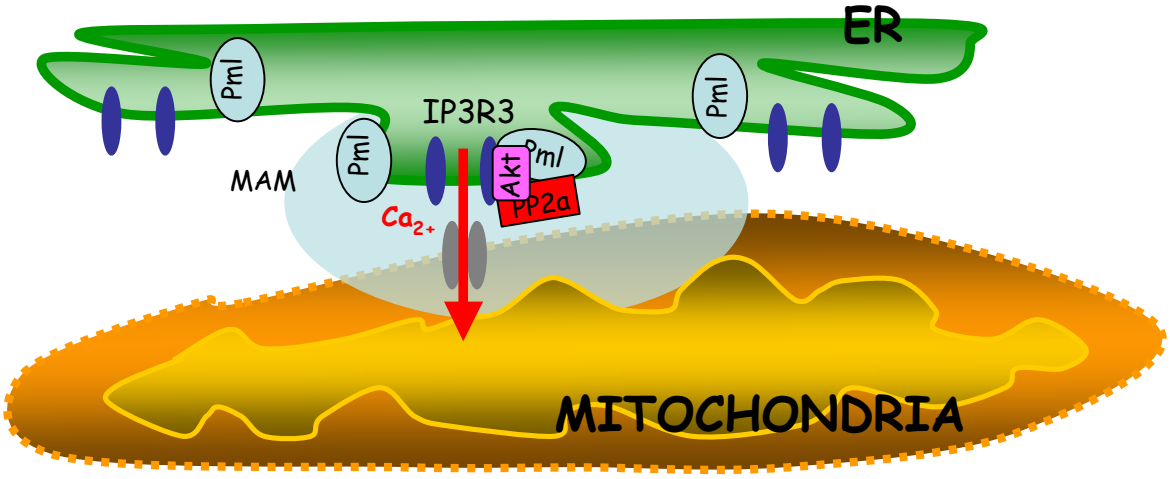

Pml $^{-/-}$